



**HAL**  
open science

## The ion-coupling mechanism of human excitatory amino acid transporters

Juan C Canul-Tec, Anand Kumar, Jonathan Dhenin, Redda Assal, Pierre Legrand, Martial Jean-Pierre Rey, Julia Chamot-Rooke, Nicolas Reyes

► **To cite this version:**

Juan C Canul-Tec, Anand Kumar, Jonathan Dhenin, Redda Assal, Pierre Legrand, et al.. The ion-coupling mechanism of human excitatory amino acid transporters. *EMBO Journal*, 2022, 41 (1), pp.377-390. 10.15252/emj.2021108341 . pasteur-03795591

**HAL Id: pasteur-03795591**

**<https://hal-pasteur.archives-ouvertes.fr/pasteur-03795591>**

Submitted on 7 Oct 2022

**HAL** is a multi-disciplinary open access archive for the deposit and dissemination of scientific research documents, whether they are published or not. The documents may come from teaching and research institutions in France or abroad, or from public or private research centers.

L'archive ouverte pluridisciplinaire **HAL**, est destinée au dépôt et à la diffusion de documents scientifiques de niveau recherche, publiés ou non, émanant des établissements d'enseignement et de recherche français ou étrangers, des laboratoires publics ou privés.



Distributed under a Creative Commons Attribution - NonCommercial | 4.0 International License

1

2

### 3 **Ion-coupling mechanism of excitatory amino acid transporters**

4 Juan C. Canul-Tec<sup>1,2,3</sup>, Anand Kumar<sup>1,2,3</sup>, Jonathan Dhenin<sup>4</sup>, Reda Assal<sup>1</sup>, Pierre  
5 Legrand<sup>5</sup>, Martial Rey<sup>4</sup>, Julia Chamot-Rooke<sup>4</sup> & Nicolas Reyes<sup>1,2,3\*</sup>

6

7 *<sup>1</sup>Membrane Protein Mechanisms Unit, Institut Pasteur, 25–28 rue du Docteur Roux,  
8 75015 Paris, France*

9 *<sup>2</sup>Membrane Protein Mechanisms Group, European Institute of Chemistry and Biology,  
10 University of Bordeaux, 2 rue Robert Escarpit 33607 Pessac, France*

11 *<sup>3</sup>CNRS UMR 5234 Fundamental microbiology and pathogenicity, Bordeaux, France*

12 *<sup>4</sup>Mass Spectrometry for Biology Unit, CNRS USR 2000, Institut Pasteur, Paris 75015,  
13 France*

14 *<sup>5</sup>Synchrotron SOLEIL, L'Orme des Merisiers, 91192 Gif-sur-Yvette, France*

15 \* Correspondence and requests for materials should be addressed to N.R.

16 (nicolas.reyes@u-bordeaux.fr)

17

18 **Abstract**

19 Human excitatory amino acid transporters (EAATs) maintain glutamate gradients in  
20 the brain essential to neurotransmission and to prevent neuronal death. They use ionic  
21 gradients as energy source, and co-transport transmitter into the cytoplasm with  $\text{Na}^+$   
22 and  $\text{H}^+$ , while counter-transport  $\text{K}^+$  to re-initiate the transport cycle. However, the  
23 molecular mechanisms underlying ion-coupled transport remain incompletely  
24 understood. Here, we present 3D structures and thermodynamic analysis of EAAT1 in  
25 different ion-bound conformations, including elusive counter-transport ion bound  
26 states. Binding energies of  $\text{Na}^+$  and  $\text{H}^+$ , and unexpectedly  $\text{Ca}^{2+}$ , are coupled to  
27 neurotransmitter binding.  $\text{Ca}^{2+}$  competes for a conserved  $\text{Na}^+$  site suggesting a  
28 regulatory role of  $\text{Ca}^{2+}$  in glutamate transport at the synapse, while  $\text{H}^+$  binds to a  
29 conserved glutamate residue stabilizing substrate occlusion. The counter-transported  
30 ion binding site overlaps with that of glutamate, revealing the  $\text{K}^+$  mechanism to exclude  
31 the transmitter during the transport cycle, and to prevent its neurotoxic release on the  
32 extracellular side.

33

34 Keywords: cryo-EM/Neurotransmitter transport/ permeation and transport/solute  
35 carrier/X-ray crystallography

36 Human excitatory amino acid transporters (EAATs) belong to the solute carrier 1  
37 (SLC1) family, and catalyze active transport of excitatory transmitters using energy  
38 stored in ionic transmembrane gradients (Erecinska *et al*, 1983; Kanner & Sharon,  
39 1978; Nelson *et al*, 1983). In each transport cycle, EAATs stoichiometrically co-  
40 transport one molecule of transmitter with 3 Na<sup>+</sup> and 1 H<sup>+</sup>, while counter-transport 1  
41 K<sup>+</sup> to re-orient the transmitter binding site to the extracellular side, and re-initiate the  
42 cycle (Barbour *et al*, 1988; Zerangue & Kavanaugh, 1996). EAAT1-2 are highly  
43 expressed on the plasma membrane of astrocytic glia (Lehre & Danbolt, 1998), where  
44 they are essential components of tripartite synapses and contribute to clear the  
45 transmitter from the cleft, as well as to regulate extracellular glutamate concentration  
46 in the brain (Zhou & Danbolt, 2014). Consistently, their dysfunctions are linked to  
47 several neurodegenerative disorders (Pajarillo *et al*, 2019).

48 SLC1 proteins are homo-trimers (Canul-Tec *et al*, 2017; Garaeva *et al*, 2018; Yernool  
49 *et al*, 2003; Yernool *et al*, 2004), and their individual subunits catalyze transport  
50 independently (Grewer *et al*, 2005; Koch & Larsson, 2005; Leary *et al*, 2007; Ruan *et al*,  
51 2017). Each subunit contains two structural and functional domains (Reyes *et al*,  
52 2009): a relatively rigid (Groeneveld & Slotboom, 2007) scaffold domain (scaD) that  
53 forms the inter-subunit interfaces; and a highly dynamic (Akyuz *et al*, 2013; Erkens *et al*,  
54 2013; Matin *et al*, 2020) transport domain (tranD) that binds substrate as well as  
55 thermodynamically-coupled ions (Boudker *et al*, 2007; Guskov *et al*, 2016; Larsson *et al*,  
56 2010; Seal & Amara, 1998; Tao *et al*, 2010; Zhang *et al*, 1998), and shuttles across  
57 the membrane in an “elevator-like” manner to translocate the cargo (Crisman *et al*,  
58 2009; Reyes *et al*, 2009).

59 Biophysical analyses of Na<sup>+</sup>-dependent EAAT archaeal homologs, Glt<sub>Ph</sub> (Boudker *et al*  
60 *et al*, 2007) and Glt<sub>TK</sub> (Guskov *et al*, 2016), showed that co-transported sodium ions bind

61 three conserved sites in the tranD (Na1-3), and that binding energy of the three co-  
62 transported Na<sup>+</sup> ions is coupled to substrate binding and occlusion, rather than directly  
63 driving its translocation (Reyes *et al.*, 2013). In the absence of substrate, two Na<sup>+</sup> bind  
64 cooperatively to Na1 and Na3, and contribute to form the substrate binding site, while  
65 subsequent binding of substrate and Na<sup>+</sup> to Na2 lead to substrate occlusion under  
66 helical-hairpin 2 (HP2) (Alleva *et al.*, 2020; Ewers *et al.*, 2013; Guskov *et al.*, 2016;  
67 Reyes *et al.*, 2013; Verdon *et al.*, 2014). HP2 dynamics controls substrate access to its  
68 binding site on opposite sides of the membrane, and HP2 closure enables elevator-like  
69 movements of the tranD, and isomerization between outward- and inward-facing states  
70 (Alleva *et al.*, 2020; Boudker *et al.*, 2007; Garaeva *et al.*, 2019; Reyes *et al.*, 2009).  
71 However, archaeal homologs are limited molecular models, as they are H<sup>+</sup> and K<sup>+</sup>  
72 independent transporters (Ryan *et al.*, 2009). Moreover, archaeal Na<sup>+</sup>-coupling  
73 mechanism has not been confirmed experimentally in EAATs. In addition, the folding  
74 instability of purified mammalian EAAT orthologs has precluded so far similar  
75 crystallographic and thermodynamic analyses of human transporters, and recent cryo-  
76 electron microscopy (cryo-EM) structures of EAAT3 fell short of revealing the  
77 complete ion-coupled mechanism (Qiu *et al.*, 2021).

78 In this work, we set out to study EAAT ion-coupled transport mechanism using  
79 thermostabilized human EAAT1 mutants, namely EAAT1<sub>CRYST</sub> and EAAT1<sub>CRYST-II</sub>  
80 (Canul-Tec *et al.*, 2017; Cirri *et al.*, 2018), as well as wild type EAAT1 (EAAT1<sub>WT</sub>).  
81 EAAT1<sub>CRYST</sub> constructs are nearly identical to EAAT1<sub>WT</sub> at the core of the tranD,  
82 where transmitter and coupled-ions bind. Consistently, they retain intact Na<sup>+</sup>, H<sup>+</sup>, and  
83 K<sup>+</sup> coupled transport mechanism after purification in detergent solutions and  
84 reconstitution in synthetic liposomes. Importantly, detergent-purified EAAT1<sub>CRYST</sub>  
85 proteins are stable under different substrate and ionic conditions, and enable both

86 thermodynamic and X-ray crystallographic analysis of the neurotransmitter transport  
87 cycle, while EAAT1<sub>WT</sub> was amenable to structural analysis by cryo-EM.

### 88 **Conserved SLC1 sodium-coupling mechanism**

89 L-glutamate uptake by purified EAAT1<sub>CRYST</sub> is strictly dependent on opposite  
90 transmembrane gradients of sodium and potassium (Canul-Tec *et al.*, 2017). To  
91 quantify binding and ion-substrate thermodynamic coupling, we measured changes in  
92 intrinsic tryptophan fluorescence of purified EAAT1<sub>CRYST</sub> in detergent solutions. Both  
93 Na<sup>+</sup> and transmitter binding, but not K<sup>+</sup>, induced robust tryptophan-fluorescence  
94 changes (> 15%) that enable titration of ligands (Fig. 1A,B). EAAT1<sub>CRYST</sub> contains two  
95 tryptophan residues, W287<sub>267</sub> in the scaD, and W473<sub>453</sub> in the tranD (herein, amino acid  
96 number refers to EAAT1<sub>WT</sub> sequence, and the corresponding number in EAAT1<sub>CRYST</sub>  
97 is in subscript). Individual phenylalanine mutants W287<sub>267</sub>F and W473<sub>453</sub>F decreased  
98 (~ 5%), and abolished, respectively, Na<sup>+</sup>/transmitter induced fluorescence signal  
99 (Appendix Figure S1A). Although the structural details underlying tryptophan  
100 fluorescence changes in EAAT1<sub>CRYST</sub> are unclear, these experiments show that the two  
101 tryptophan residues are required to probe Na<sup>+</sup> binding, and that changes in tranD  
102 dynamics induced by Na<sup>+</sup> and K<sup>+</sup> binding are significantly different.

103 In the absence of substrate, sodium ions bind EAAT1<sub>CRYST</sub> in a cooperative manner  
104 with an apparent dissociation constant ( $K_D$ ) of  $21.6 \pm 0.4$  mM, and a hill coefficient  
105 ( $n_H$ ) of  $2.2 \pm 0.1$  (Fig. 1C), consistent with binding of two sodium ions to the apo tranD  
106 at Na1 and Na3. In agreement with this, asparagine mutation of strictly conserved  
107 D400<sub>380</sub> in Na3 greatly impaired sodium binding ( $K_D > 100$  mM). Moreover, in the  
108 presence of allosteric inhibitor UCPH<sub>101</sub> (Jensen *et al.*, 2009), which traps the  
109 transporters in outward-facing states (Canul-Tec *et al.*, 2017), Na<sup>+</sup> titrations of  
110 EAAT1<sub>CRYST</sub> yielded similar binding parameters ( $K_D = 14.6 \pm 0.3$  mM;  $n_H = 1.6 \pm 0.1$ ).

111 These results indicate that tryptophan-fluorescence changes report on conformational  
112 changes associated to binding, rather than membrane translocation of the tranD, and  
113 further that Na<sup>+</sup> binds outward- and inward facing states with comparable affinities.  
114 Substrate binding to EAAT1<sub>CRYST</sub> was strongly sodium-dependent, and the logarithmic  
115 plot of the substrate K<sub>D</sub> versus sodium concentration yielded a straight line with a slope,  
116 or coupling efficiency (C<sub>E</sub>) value of  $-2.6 \pm 0.3$  (Fig. 1D). C<sub>E</sub> is the apparent number of  
117 ions thermodynamically coupled to binding of one substrate molecule, and our results  
118 show that in EAAT1<sub>CRYST</sub> the binding energy of the three co-transported sodium ions  
119 is coupled to neurotransmitter binding. Moreover, at 1 mM Na<sup>+</sup>, transmitter K<sub>D</sub> values  
120 in the presence ( $0.9 \pm 0.1$  mM) and absence of UCPH<sub>101</sub> ( $2.8 \pm 0.8$  mM) were  
121 comparable.

122 Indeed, similarities in Na<sup>+</sup>, and Na<sup>+</sup>-transmitter coupled binding properties between  
123 archaeal homologs (Reyes *et al.*, 2013) and EAAT1<sub>CRYST</sub> strongly suggests  
124 conservation of the Na<sup>+</sup>-coupling mechanism.

125 To gain structural insight on the location of the sodium binding sites, we extended the  
126 reported crystallographic atomic model of Na<sup>+</sup>/transmitter bound EAAT1<sub>CRYST</sub> (Canul-  
127 Tec *et al.*, 2017) in complex with UCPH<sub>101</sub> (see methods). Notably, the extended model  
128 includes an N-terminal helix that lies nearly parallel to the membrane plane (TM1a'),  
129 and has not been noted before in structures of SLC1 proteins (Fig. 2A,B). Interestingly,  
130 amino acid deletions in this region slow down substrate uptake by EAAT1<sub>WT</sub> expressed  
131 in cells (Appendix Figure S1B), suggesting a modulatory role of TM1a' on transport  
132 kinetics. Notably, EAAT1<sub>CRYST</sub> Fo-Fc electron density map omitting sodium ions  
133 shows three distinct density peaks ( $> 4\sigma$ ) within the tranD (Fig. 2C). Several lines of  
134 structural and functional evidence indicate that the observed peaks correspond to three  
135 co-transported Na<sup>+</sup> bound to the tranD: the peaks accurately localize to the three

136 conserved sodium binding sites (Na1-Na3) previously observed in X-ray structures of  
137 archaeal homologs (Alleva *et al.*, 2020; Boudker *et al.*, 2007; Guskov *et al.*, 2016).  
138 Accordingly, three sodium ions modeled in EAAT1<sub>CRYST</sub> structure reveal nearly  
139 identical coordination compared to the homologs (Fig. 2D); ion coordination in  
140 EAAT1<sub>CRYST</sub> at the three sites is exclusively done by oxygen atoms, as expected for a  
141 weak acid like Na<sup>+</sup>, while water coordination is expected to have additional  
142 contributions by nitrogen atoms, reflecting its H-bonding capacity (Nayal & Di Cera,  
143 1996); Finally, reported mutagenesis of residues that contribute side chains to Na1 and  
144 Na3, including D400<sub>380</sub>N (Fig. 1C), impaired Na<sup>+</sup>-dependent function in both EAATs  
145 and prokaryotic homologs (Bastug *et al.*, 2012; Boudker *et al.*, 2007; Tao *et al.*, 2010).  
146 Overall, the above structural and thermodynamic results are in excellent agreement with  
147 the sodium-coupling mechanism of archaeal transporters (Alleva *et al.*, 2020; Ewers *et*  
148 *al.*, 2013; Guskov *et al.*, 2016; Reyes *et al.*, 2013; Verdon *et al.*, 2014), and confirm its  
149 conservation in human SLC1 proteins. In this mechanism, cooperative Na<sup>+</sup> binding to  
150 apo transporters leads to occupancy of Na1 and Na3 sites and contributes to the  
151 formation of the substrate binding site, while subsequent binding of substrate and Na<sup>+</sup>  
152 to Na2 lead to substrate occlusion under HP2, and enables transmembrane movements  
153 of the tranD. Na<sup>+</sup>, as well as Na<sup>+</sup>-transmitter coupled binding affinities to outward- and  
154 inward-facing states are similar.

### 155 **Proton coupling**

156 L-glutamate uptake by purified EAAT1<sub>CRYST</sub> decreases steeply at basic pH values (Fig.  
157 3A), resembling transport pH-dependence observed in EAAT mammalian orthologs  
158 expressed in cells (Watzke *et al.*, 2000; Zerangue & Kavanaugh, 1996), and  
159 demonstrating that the proton-coupled transport mechanism of the thermostable mutant  
160 is intact.



161 To gain thermodynamic insight on this mechanism, we measured Na<sup>+</sup>, as well as  
162 Na<sup>+</sup>/transmitter coupled binding to apo transporters as a function of pH using the  
163 tryptophan-fluorescence assay. There was no significant change in Na<sup>+</sup> apparent K<sub>D</sub> in  
164 a pH range from 6 to 10 (C<sub>E</sub> = 0.09 ± 0.03), while substrate K<sub>D</sub> significantly increased  
165 with pH (C<sub>E</sub>=0.55 ± 0.02) at constant [Na<sup>+</sup>] (Fig. 3B). These results demonstrate that  
166 neurotransmitter binding is thermodynamically coupled to binding of one H<sup>+</sup>, and argue  
167 that cooperative Na<sup>+</sup> binding to apo transporters, at Na1 and Na3, is H<sup>+</sup>-uncoupled. We  
168 next asked if the apo transporters are able to bind protons. Indeed, total tryptophan-  
169 fluorescence changes associated to saturating Na<sup>+</sup>/transmitter coupled binding  
170 significantly decreased at pH values below neutral (Fig. EV1A,B), indicating that  
171 protons change tryptophan-fluorescence of apo transporter upon binding.

172 To find ionizable side chains that could act as proton acceptors in the tranD, we  
173 compared amino acid sequences from representative vertebrate species of two divergent  
174 branches of SLC1 transporters (Gesemann *et al*, 2010): pH-dependent EAATs, and pH-  
175 independent neutral amino acid exchangers (so-called ASCTs) (Fig. EV1C,D). The  
176 tranD of EAAT1<sub>CRYST</sub> contains over 30 ionizable side chains, but only Y127<sub>127</sub> (TM3),  
177 Y405<sub>385</sub> (TM7b), E406<sub>386</sub> (TM7b), and R479<sub>459</sub> (TM8b) are strictly conserved among  
178 EAAT orthologs, and not among ASCT ones. R479<sub>459</sub> is in close proximity to  
179 conserved acidic residues (E406<sub>386</sub>, D472<sub>452</sub>, and D476<sub>456</sub>), while Y127<sub>127</sub> backbone is  
180 part of Na3, where Na<sup>+</sup> arguably binds in a pH-independent fashion. Hence, it is highly  
181 unlikely that those two residues exchange protons with the bulk during the transport  
182 cycle, and we focused our analysis on Y405<sub>385</sub> and E406<sub>386</sub>. Indeed, conservative single  
183 mutations bearing non-ionizable sidechains had minor effects on pH-dependence of  
184 substrate binding in Y405<sub>385</sub>F (C<sub>E</sub>=0.37 ± 0.06), but abolished this dependence in  
185 E406<sub>386</sub>Q (C<sub>E</sub>=0.00 ± 0.04) (Fig. 3C). Our results agree well with early studies of rodent

186 ortholog EAAC1 showing that equivalent mutation to E406<sub>386</sub>Q (E373Q) impairs pH-  
187 dependence of apparent glutamate-binding (Grewer *et al*, 2003), as well as with  
188 molecular dynamic simulations of transmitter binding (Heinzelmann & Kuyucak,  
189 2014), and support the role of E406 carboxylate as the main proton acceptor in the  
190 transport cycle.

191 From a structural viewpoint, E406<sub>386</sub> sidechain is occluded within the tranD core at  
192 hydrogen-bond distance of G447<sub>427</sub> backbone-carbonyl oxygen, T450<sub>430</sub> sidechain  
193 hydroxyl, and M451<sub>431</sub> backbone amide in HP2b in the Na<sup>+</sup>/transmitter-bound  
194 EAAT1<sub>CRYST</sub> structure (Fig. 3D). Consistent with its proton acceptor role, protonation  
195 of E406<sub>386</sub> carboxylate group would expand its H-bonding capacity and enable  
196 formation of a H-bond network with HP2b, contributing to maintain HP2 in a close  
197 position with substrate occluded underneath, and explaining at least partly the  
198 thermodynamic coupling between H<sup>+</sup> and transmitter binding. Because it is not possible  
199 to determine the protonation state of amino acid sidechains in the EAAT1<sub>CRYST</sub> crystal  
200 structure, we determined the structure of EAAT1<sub>CRYST</sub>-E406<sub>386</sub>Q mutant, mimicking  
201 the protonated state of E406<sub>386</sub>. Indeed, the position of E406<sub>386</sub>Q side chain is identical  
202 within experimental error to that of E406<sub>386</sub> (Appendix Figure S2A,B), consistent with  
203 E406<sub>386</sub> being protonated in the Na<sup>+</sup>/transmitter-bound state.

204 All functional and structural results converge to show that Na<sup>+</sup>/transmitter bound  
205 structure represents the transmitter translocation complex of the tranD with 3 Na<sup>+</sup>, 1  
206 H<sup>+</sup>, and 1 neurotransmitter molecule bound.

### 207 **Counter-transported ion binding-site**

208 To understand the structural basis underlying ion counter-transport in EAATs, we  
209 solved the crystal structure of transporters purified in Rb<sup>+</sup>-based buffer, in the absence  
210 of Na<sup>+</sup> and transmitter, and in complex with UCPH<sub>101</sub>. Rb<sup>+</sup> is a K<sup>+</sup> analog, and the

211 advantage for crystallographic experiments is that Rb<sup>+</sup> yields robust anomalous X-ray  
212 scattering signals to unambiguously determine the position of bound ion(s) to the  
213 transporter, at the resolution of our structure (~3.9 Å). Importantly, liposome uptake  
214 experiments show that Rb<sup>+</sup> is counter-transported by EAAT1<sub>CRYST</sub>, demonstrating that  
215 it is a functional K<sup>+</sup> analog for EAAT1 structural studies (Fig. 4A).

216 Rb<sup>+</sup> and UCPH<sub>101</sub> bound EAAT1<sub>CRYST</sub> structure adopts an outward-facing open state,  
217 and the anomalous difference map with the X-ray beam tuned at a Rb<sup>+</sup> absorption  
218 maximum (0.815 Å) shows two anomalous-difference peaks (> 5σ), namely P1 and P2.  
219 P1 localizes to the substrate binding site near conserved D476<sub>456</sub>, and P2 to Na3 (Fig.  
220 4B). As negative control, we collected diffraction data from a similar crystal, but with  
221 the X-ray beam tuned off the Rb<sup>+</sup>-absorption maximum (0.998 Å), and observed P2 (>  
222 5σ), but not P1 in the anomalous-difference map (Fig. EV2). These results demonstrate  
223 that Rb<sup>+</sup>, a functional counter-transported ion by EAAT1, is bound to the transporter at  
224 the substrate binding site. Notably, this counter-transported ion binding site, namely  
225 K<sub>CT</sub>, overlaps with the position of the substrate amide-nitrogen atom in the  
226 Na<sup>+</sup>/transmitter-bound structure, and it is coordinated by the carboxylate side chain of  
227 D476<sub>456</sub> (TM8b), backbone carbonyl oxygen of S363<sub>343</sub> (HP1), and possibly its  
228 sidechain, as well as that of T480<sub>460</sub> (TM8b) and water molecules (Fig. 4B). The  
229 striking overlap with the transmitter binding site makes K<sub>CT</sub> an optimal site for the  
230 counter-transported ion to exclude the transmitter during the transport cycle.

231 Consistently, early computational (Holley & Kavanaugh, 2009), functional (Wang *et*  
232 *al.*, 2013) and crystallographic (Verdon *et al.*, 2014) studies of EAAT homologs  
233 predicted mutually exclusive transmitter and K<sup>+</sup> binding sites at similar positions.

234 **Calcium binding to Na3 site**

235 Our anomalous scattering analysis reveals a second ion bound to Na3 in the Rb<sup>+</sup> bound  
236 EAAT1<sub>CRYST</sub> structure. In addition to Rb<sup>+</sup> (at ~100 mM), crystallization conditions  
237 contain Ba<sup>2+</sup> and Ca<sup>2+</sup> (at ~25 mM), and only the former could generate significant  
238 anomalous peaks off the Rb<sup>+</sup> absorption maximum (0.998 Å). To shed light on this  
239 problem, we solved the structure of transporters purified in the absence of substrate,  
240 Na<sup>+</sup>, and Rb<sup>+</sup>, and using choline as a substitute for monovalent cations, but otherwise  
241 under similar crystallization conditions containing Ba<sup>2+</sup> and Ca<sup>2+</sup>. In these crystals, we  
242 found a single anomalous-difference peak that corresponds to P2 (> 8σ) at Na3 (Fig.  
243 5A), consistent with Ba<sup>2+</sup> binding at this sodium site. From a structural point of view,  
244 Ba<sup>2+</sup> binding to Na3 would be possible through conformational changes around the  
245 <sup>398</sup>NMDG motif, particularly at the level of N398<sub>378</sub> that moves away from the center  
246 of the site compared to the transmitter bound structure, enabling occupancy by a larger  
247 cation than Na<sup>+</sup> (Fig. EV3).

248 From a functional perspective, Ba<sup>2+</sup> binding to a conserved Na<sup>+</sup>-binding site in EAATs  
249 raises the interesting possibility that physiologically-relevant analog Ca<sup>2+</sup> would also  
250 bind there. Ca<sup>2+</sup> and Ba<sup>2+</sup> binding to EAAT1<sub>CRYST</sub> transporters was confirmed by  
251 changes in intrinsic-tryptophan fluorescence, and showed several important features:  
252 Ca<sup>2+</sup> binds apo transporters with K<sub>D</sub> = 2.9 ± 0.4 mM in a non-cooperative manner (n<sub>H</sub>  
253 = 0.9 ± 0.1), and mutation D400<sub>380</sub>N increased its K<sub>D</sub> by at least an order of magnitude  
254 (Fig. 5B), consistent with binding of one calcium ion to Na3; Ca<sup>2+</sup> binding parameters  
255 were not significantly affected by allosteric inhibitor UCPH<sub>101</sub> (K<sub>D</sub> = 1.4 ± 0.1 mM;  
256 n<sub>H</sub> = 0.9 ± 0.03), implying that Ca<sup>2+</sup> affinities to outward- and inward-facing states are  
257 comparable; Ca<sup>2+</sup> (and Ba<sup>2+</sup>), but not K<sup>+</sup> significantly increased Na<sup>+</sup> apparent K<sub>D</sub> (Fig.  
258 EV4), indicating competitive binding between Ca<sup>2+</sup> (or Ba<sup>2+</sup>) and Na<sup>+</sup>, as well as lack  
259 of K<sup>+</sup> affinity for Na1 and Na3; binding of substrate was thermodynamically coupled

260 to one  $\text{Ca}^{2+}$  ( $C_E = -0.8 \pm 0.1$ ) (Fig. 5C), as expected for a cation that binds to Na3. In  
261 addition, reconstituted transmitter uptake in liposomes demonstrates that  $\text{Ca}^{2+}$  is not  
262 counter-transported (Fig. 4A), at least not at rates comparable to  $\text{K}^+$  or  $\text{Rb}^+$ , suggesting  
263 that a cation bound to Na3 is not able to form a translocation complex to re-locate the  
264 substrate binding site. However,  $\text{Ca}^{2+}$  weakly inhibited transport with half-maximal  
265 inhibitory concentrations ( $\text{IC}_{50}$ )  $\sim 5$  mM, when added to  $\text{K}^+$ -containing intra-liposomal  
266 side, but it lacked effect when added to the  $\text{Na}^+$ /transmitter-containing extracellular  
267 solution in cells (Fig. EV5A,B). Lack of extracellular  $\text{Ca}^{2+}$  effect on steady-state  
268 transport is likely due to competition to much stronger  $\text{Na}^+/\text{H}^+$ /transmitter coupled  
269 binding, while intra-liposomal  $\text{Ca}^{2+}$  inhibition could be due to facilitation of transmitter  
270 re-binding inside the liposome, as  $\text{Ca}^{2+}$  and transmitter binding are thermodynamically  
271 coupled.

272 From a physiological perspective,  $\text{Ca}^{2+}$ /transmitter coupling could play a regulatory  
273 role of  $\text{Ca}^{2+}$  in glutamate transport at tripartite synapses. Fine astrocytic processes at  
274 the synapse undergo transient increases in intracellular  $[\text{Ca}^{2+}]$  ( $[\text{Ca}^{2+}]_i$ ), and modulate  
275 neuronal activity by increasing the amount of extracellular neurotransmitter available  
276 (Bazargani & Attwell, 2016). One potential mechanism linking these two phenomena  
277 is that at physiological glutamate intracellular-concentrations in astrocytes (mM),  
278  $[\text{Ca}^{2+}]_i$  transients could promote re-binding of the transmitter to EAATs, slowing down  
279 glutamate transport and increasing the amount of transmitter available at the synapse.  
280 Testing that and other hypotheses regarding the effect of extra- and/or intracellular  $\text{Ca}^{2+}$   
281 on transmitter transport will require further experimentation, including time-resolved  
282 techniques.

283 **Conformational changes associated to ion counter transport**

284 Rb<sup>+</sup>/Ba<sup>2+</sup> bound EAAT1<sub>CRYST</sub> structure shows extensive and concerted conformational  
285 changes on the extracellular half of the tranD compared to the Na<sup>+</sup>/transmitter bound  
286 state (Fig. 4B). The helical arms of HP2 and TM8a, and to a lesser extent the  
287 extracellular part of TM3, TM6, and TM7 move outward and towards the scaD, while  
288 the tip of HP2 is in an open position stabilized by a ~90-degree rotation of M399<sub>379</sub>  
289 sidechain towards the extracellular side, and separated from the tip of HP1 by as much  
290 as ~11 Å. These movements expose the tranD core to the bulk, and enable hydration of  
291 transmitter, Na<sup>+</sup>, and H<sup>+</sup> binding sites, as well as distort sodium and transmitter  
292 coordination (Fig. EV3): backbone and sidechain movements of N398<sub>378</sub> and M399<sub>379</sub>,  
293 at the conserved <sup>398</sup>NMDG motif, break Na<sup>+</sup> coordination at Na1-3, while those of HP2,  
294 T402<sub>382</sub>, and R479<sub>459</sub> disrupt transmitter's binding site.

295 The outward-facing open states seen in the structures of apo transporters (Rb<sup>+</sup>/Ba<sup>2+</sup> and  
296 Ba<sup>2+</sup> bound, respectively) are nearly identical (Fig. 5A), suggesting that the presence of  
297 divalent cations in the crystallization buffer and/or crystal contacts might restrict  
298 conformational changes of the tranD. Moreover, the open position of HP2 should  
299 preclude transmembrane movements of the tranD and therefore, these structures likely  
300 represent intermediates of the transport cycle that do not correspond to the K<sup>+</sup>  
301 translocation complex. To overcome these limitations, we determined the cryo-EM  
302 structure of EAAT1<sub>WT</sub> purified in a K<sup>+</sup>-based buffer (in the absence of other  
303 monovalent and divalent coupled cations, as well as transmitter and UCPH<sub>101</sub>) at an  
304 overall ~ 4.0 Å resolution (Fig. 6A and Appendix Figure S3). The quality of the cryo-  
305 EM map was better in the scaD than in tranD, likely reflecting the dynamic nature of  
306 the latter (Appendix Figure S4), and we observed non-protein density for lipid or  
307 detergent molecules at the scaD-tranD, as well as at inter-subunit interfaces suggesting  
308 a regulatory role of lipids in tranD dynamics and trimer stability, respectively.

309 The cryo-EM structure shows a symmetric EAAT1<sub>WT</sub> trimer in an inward-facing state  
310 with TM1a and TM1a' laying nearly parallel to the membrane, as well as two long beta-  
311 strands between TM4b-c in the scaD protruding outside the membrane plane,  
312 resembling the ones observed in human ASCT2 (Garaeva *et al.*, 2018). Consistent with  
313 an elevator-like mechanism, the entire tranD undergoes a large movement that  
314 translocates ligand binding-sites across the membrane, moving them by as much as 18  
315 Å into the cytoplasmic side (Fig. 6B). Notably, tranD backbone adopts a different  
316 conformation compared to that in Na<sup>+</sup>/transmitter and Rb<sup>+</sup>/Ba<sup>2+</sup> crystal structures,  
317 respectively (Fig. 6C). The extracellular half of the tranD, including HP2 and TM8a,  
318 moves outward and towards the scaD expanding the tranD core compared to the  
319 Na<sup>+</sup>/transmitter bound state, but to a lesser extent than in the Rb<sup>+</sup>/Ba<sup>2+</sup> bound state. In  
320 the cytoplasmic part of the tranD, TM7a moves away from HP1b at the level of Na1.  
321 Yet, the tip of HP2 remains in contact with that of HP1 in a close position. The  
322 concerted backbone movements of the tranD have several important mechanistic  
323 implications: separation of HP2a, HP1b, and TM7a away from each other disrupts  
324 backbone-atom coordination at Na1, Na2, and transmitter binding sites; concomitantly,  
325 close proximity of HP1 and HP2 tips suggests that backbone carbonyl oxygen atoms of  
326 I423<sub>403</sub> and/or P424<sub>404</sub> (HP2 tip) could contribute to counter-transported ion  
327 coordination and occlusion at K<sub>CT</sub> and therefore, that the tranD adopts an occluded state  
328 competent for K<sup>+</sup> translocation.

329 To gain further insight into K<sup>+</sup>-induced conformational changes outside the context of  
330 the crystal lattice, we compared hydrogen-deuterium exchange linked to mass  
331 spectrometry (HDX-MS) profiles of transporters at 25°C in Na<sup>+</sup>/transmitter, and K<sup>+</sup>  
332 buffers, respectively (Fig. 6D and Appendix Figure S5, S6). EAAT1<sub>WT</sub> was not  
333 amenable to HDX-MS analysis due rapid and irreversible unfolding at 25°C (Cirri *et*

334 *al.*, 2018). Hence, we probed thermostabilized EAAT1<sub>CRYST</sub> using short deuterium-  
335 labeling time (1 min) to avoid unfolding events, and in the presence of UCPH<sub>101</sub> to  
336 restrict the conformational sampling to outward-facing states. Indeed, transporters in  
337 K<sup>+</sup> compared to Na<sup>+</sup>/transmitter buffers showed a significant increase in HDX that  
338 localizes to the tip of HP1 and HP2, as well as the NMDG motif. These regions lack  
339 secondary structure, in both transmitter and counter-transported ion bound states, and  
340 contain key residues for Na<sup>+</sup> and transmitter coordination. Therefore, the observed  
341 changes in HDX imply that K<sup>+</sup> induces a significant increase in backbone hydration  
342 around the ligand binding sites, which is in excellent agreement with the  
343 conformational expansion of the tranD core observed in both crystal and cryoEM  
344 structures of apo transporters. Importantly, K<sup>+</sup>-induced HDX changes reverted fully  
345 upon adding back Na<sup>+</sup>/transmitter (Appendix Figure S6, control condition),  
346 demonstrating that transporters remain folded and respond to addition of ligands, and  
347 that observed HDX changes were not due to unfolding events of purified protein  
348 assayed at 25°C.

#### 349 **Discussion**

350 Based on our structural and thermodynamic analyses, we propose a complete Na<sup>+</sup>, H<sup>+</sup>,  
351 K<sup>+</sup> coupled neurotransmitter transport mechanism that unifies a wealth of structural and  
352 biophysical data on SLC1 proteins (Fig. 7). In this mechanism, Na<sup>+</sup> binding to Na1-  
353 Na3 and protonation of E406<sub>386</sub> are thermodynamically coupled to transmitter binding  
354 and occlusion, and lead to the formation of the transmitter translocation complex,  
355 represented by EAAT1<sub>CRYST</sub> Na<sup>+</sup>/transmitter bound crystal structure (Fig. 2A-D). In  
356 turn, K<sup>+</sup> binding to K<sub>CT</sub> promotes self-occlusion, and formation of a K<sup>+</sup> translocation  
357 complex that excludes the transmitter, and it is represented by EAAT1<sub>WT</sub> cryo-EM  
358 structure (Fig. 6A,B).



359 Cooperative Na<sup>+</sup> binding to Na1 and Na3 in apo EAAT1<sub>CRYST</sub> enables substrate binding  
360 through re-arrangements of the NMDG signature motif that resemble those observed in  
361 SLC1 archaeal homologs (Guskov *et al.*, 2016; Verdon *et al.*, 2014), and this process  
362 is independent of both H<sup>+</sup> and K<sup>+</sup>. Sodium-saturated apo-transporters undergo three key  
363 thermodynamically-coupled events that lead to substrate occlusion under HP2, and the  
364 formation of transmitter translocation complex: Na<sup>+</sup> binding to Na2 stabilizes HP2a  
365 against TM7a; protonation of E406<sub>386</sub> in TM7b enables hydrogen-bonding with HP2b;  
366 and transmitter binding secures closure of HP2 tip through direct coordination.

367 What are then the events that lead to formation of the K<sup>+</sup> translocation complex? Our  
368 results demonstrate counter-transported ion binding to K<sub>CT</sub>, as well as hydration of the  
369 tranD core associated to K<sup>+</sup>, strongly suggesting that these are key events to form the  
370 translocation complex. Importantly, K<sub>CT</sub> fulfills two essential requirements as counter-  
371 transported ion binding site, first it precludes transmitter binding preventing futile  
372 transport cycles and potentially-cytotoxic release of glutamate and second, it promotes  
373 formation of a competent occluded state that enables elevator-like movements of the  
374 tranD, as suggested by the closed position of HP2 in EAAT1<sub>WT</sub> cryo-EM structure.

375 Early reports predicted counter-transported ion binding sites similar to K<sub>CT</sub> and  
376 mutually-exclusive transmitter and K<sup>+</sup> binding mechanisms (Holley & Kavanaugh,  
377 2009; Verdon *et al.*, 2014; Wang *et al.*, 2013), in excellent agreement with our results.

378 However, this view has been challenged by computational and functional studies that  
379 highlighted the role of Na1, as a likely counter-transported ion binding site (Kortzak *et*  
380 *al.*, 2019; Wang *et al.*, 2020). Several lines of experimental evidence presented here  
381 argue against that proposal: first, crystals grown in ~100 mM counter-transported ion  
382 (Rb<sup>+</sup>) do not show anomalous-scattering peaks at Na1, revealing lack of ion occupancy  
383 at this site (Fig. 4B and Fig. EV2); second, K<sup>+</sup> concentrations up to 1.5 M have no

384 significant effect on cooperative Na<sup>+</sup> binding to apo transporters, arguably at Na1 and  
385 Na3, consistent with lack of K<sup>+</sup> affinity for these sites. Moreover, Ca<sup>2+</sup> binds to Na3  
386 with a K<sub>D</sub> value in the low mM range, and induces a large increase in Na<sup>+</sup> apparent K<sub>D</sub>  
387 (Fig. EV4). This supports the intuitive idea that significant occupancy of sodium sites  
388 by other cations impacts the apparent Na<sup>+</sup>-binding parameter. Finally, in EAAT1<sub>WT</sub>  
389 cryo-EM structure, solved in the presence of 100 mM K<sup>+</sup> and absence of divalent  
390 cations, backbone movements of TM7a away from HP1 distort Na1 geometry, and it is  
391 not consistent with ion coordination at this site (Fig. 6C).

392 The close proximity of conserved R479<sub>459</sub> to K<sub>CT</sub> argues that electrostatic shielding of  
393 its sidechain is required for K<sup>+</sup> occlusion and translocation, as suggested by reported  
394 apo EAAT3 structure (Qiu *et al.*, 2021) and MD simulations (Kortzak *et al.*, 2019), and  
395 hydration of the tranD core is likely key to this process. Both our crystal and cryo-EM  
396 structures of apo transporters show expansions of the tranD core around the ligand  
397 binding sites, and HDX-MS experiments confirmed increased hydration in this region.  
398 Water penetration in the tranD core should directly contribute to shield R479<sub>459</sub> charge,  
399 and more importantly induce deprotonation of E406<sub>386</sub>, enabling ionic interactions  
400 between the two residues. Hydrogen-bonding between R479<sub>459</sub> and T402<sub>382</sub> could also  
401 contribute to electrostatic shielding (Fig. 4B). Consistently, E406<sub>386</sub> and T402<sub>382</sub> are  
402 highly conserved in EAAT orthologs, but are glutamine and alanine, respectively, in  
403 ASCT ones. Therefore, we propose a dual role of E406<sub>386</sub> and R479<sub>459</sub> in transport: in  
404 the transmitter translocation complex protonated E406<sub>386</sub> contributes to transmitter  
405 occlusion through hydrogen bonding with HP2, while R479<sub>459</sub> coordinates the gamma  
406 carboxylate group of the substrate. In the K<sup>+</sup> translocation complex, deprotonated  
407 E406<sub>386</sub> engages in ionic interactions with R479<sub>459</sub>, enabling K<sup>+</sup> occlusion at K<sub>CT</sub>.  
408 Equivalent mutations to E406Q in mammalian orthologs impair both H<sup>+</sup> and K<sup>+</sup>

409 coupled transmitter transport (Greuer *et al.*, 2003; Kavanaugh *et al.*, 1997), further  
410 supporting the dual role of E406 in H<sup>+</sup> and K<sup>+</sup> coupling. Moreover, the cryo-EM  
411 structure of inwardly-open EAAT3 in apo conditions shows equivalent residues to  
412 E406 and R479 forming a salt bridge, although their roles in substrate occlusion seem  
413 different (Qiu *et al.*, 2021), likely reflecting evolutionary differences among EAAT  
414 isoforms.

415 Our findings shed light on controversial and important aspects of EAATs transport  
416 cycle, and suggest novel mechanisms to regulate glutamate levels at tripartite synapses.

417

418 **Conflict of interest**

419 The authors declare no competing financial interests.

420

421  
422  
423  
424  
425  
426  
427  
428  
429  
430  
431  
432  
433  
434  
435  
436  
437  
438  
439  
440  
441  
442  
443  
444  
445  
446  
447  
448  
449  
450  
451  
452  
453  
454  
455  
456  
457  
458  
459  
460  
461  
462  
463  
464  
465  
466  
467  
468

## References

- Adams PD, Afonine PV, Bunkoczi G, Chen VB, Davis IW, Echols N, Headd JJ, Hung LW, Kapral GJ, Grosse-Kunstleve RW *et al* (2010) PHENIX: a comprehensive Python-based system for macromolecular structure solution. *Acta Crystallogr D Biol Crystallogr* 66: 213-221
- Akyuz N, Altman RB, Blanchard SC, Boudker O (2013) Transport dynamics in a glutamate transporter homologue. *Nature* 502: 114-118
- Alleva C, Kovalev K, Astashkin R, Berndt MI, Baeken C, Balandin T, Gordeliy V, Fahlke C, Machtens JP (2020) Na(+)-dependent gate dynamics and electrostatic attraction ensure substrate coupling in glutamate transporters. *Sci Adv* 6
- Barbour B, Brew H, Attwell D (1988) Electrogenic glutamate uptake in glial cells is activated by intracellular potassium. *Nature* 335: 433-435
- Bastug T, Heinzelmann G, Kuyucak S, Salim M, Vandenberg RJ, Ryan RM (2012) Position of the third Na<sup>+</sup> site in the aspartate transporter GltPh and the human glutamate transporter, EAAT1. *PLoS One* 7: e33058
- Bazargani N, Attwell D (2016) Astrocyte calcium signaling: the third wave. *Nat Neurosci* 19: 182-189
- Blanc E, Roversi P, Vornrhein C, Flensburg C, Lea SM, Bricogne G (2004) Refinement of severely incomplete structures with maximum likelihood in BUSTER-TNT. *Acta Crystallogr D Biol Crystallogr* 60: 2210-2221
- Boudker O, Ryan RM, Yernool D, Shimamoto K, Gouaux E (2007) Coupling substrate and ion binding to extracellular gate of a sodium-dependent aspartate transporter. *Nature* 445: 387-393
- Canul-Tec JC, Assal R, Cirri E, Legrand P, Brier S, Chamot-Rooke J, Reyes N (2017) Structure and allosteric inhibition of excitatory amino acid transporter 1. *Nature* 544: 446-451
- Chen VB, Arendall WB, 3rd, Headd JJ, Keedy DA, Immormino RM, Kapral GJ, Murray LW, Richardson JS, Richardson DC (2010) MolProbity: all-atom structure validation for macromolecular crystallography. *Acta Crystallogr D Biol Crystallogr* 66: 12-21
- Cirri E, Brier S, Assal R, Canul-Tec JC, Chamot-Rooke J, Reyes N (2018) Consensus designs and thermal stability determinants of a human glutamate transporter. *Elife* 7
- Crisman TJ, Qu S, Kanner BI, Forrest LR (2009) Inward-facing conformation of glutamate transporters as revealed by their inverted-topology structural repeats. *Proc Natl Acad Sci U S A* 106: 20752-20757
- Emsley P, Lohkamp B, Scott WG, Cowtan K (2010) Features and development of Coot. *Acta Crystallogr D Biol Crystallogr* 66: 486-501
- Erecinska M, Wantorsky D, Wilson DF (1983) Aspartate transport in synaptosomes from rat brain. *J Biol Chem* 258: 9069-9077
- Erkens GB, Hanelt I, Goudsmits JM, Slotboom DJ, van Oijen AM (2013) Unsynchronised subunit motion in single trimeric sodium-coupled aspartate transporters. *Nature* 502: 119-123
- Evans PR, Murshudov GN (2013) How good are my data and what is the resolution? *Acta Crystallogr D Biol Crystallogr* 69: 1204-1214
- Ewers D, Becher T, Machtens JP, Weyand I, Fahlke C (2013) Induced fit substrate binding to an archeal glutamate transporter homologue. *Proc Natl Acad Sci U S A* 110: 12486-12491

469 Garaeva AA, Guskov A, Slotboom DJ, Paulino C (2019) A one-gate elevator  
470 mechanism for the human neutral amino acid transporter ASCT2. *Nat Commun* 10:  
471 3427

472 Garaeva AA, Oostergetel GT, Gati C, Guskov A, Paulino C, Slotboom DJ (2018) Cryo-  
473 EM structure of the human neutral amino acid transporter ASCT2. *Nat Struct Mol Biol*  
474 25: 515-521

475 Gesemann M, Lesslauer A, Maurer CM, Schonhaler HB, Neuhauss SC (2010)  
476 Phylogenetic analysis of the vertebrate excitatory/neutral amino acid transporter  
477 (SLC1/EAAT) family reveals lineage specific subfamilies. *BMC Evol Biol* 10: 117

478 Goddard TD, Huang CC, Meng EC, Pettersen EF, Couch GS, Morris JH, Ferrin TE  
479 (2018) UCSF ChimeraX: Meeting modern challenges in visualization and analysis.  
480 *Protein Sci* 27: 14-25

481 Grewer C, Balani P, Weidenfeller C, Bartusel T, Tao Z, Rauen T (2005) Individual  
482 subunits of the glutamate transporter EAAC1 homotrimer function independently of  
483 each other. *Biochemistry* 44: 11913-11923

484 Grewer C, Watzke N, Rauen T, Bicho A (2003) Is the glutamate residue Glu-373 the  
485 proton acceptor of the excitatory amino acid carrier 1? *J Biol Chem* 278: 2585-2592

486 Groeneveld M, Slotboom DJ (2007) Rigidity of the subunit interfaces of the trimeric  
487 glutamate transporter GltT during translocation. *J Mol Biol* 372: 565-570

488 Guskov A, Jensen S, Faustino I, Marrink SJ, Slotboom DJ (2016) Coupled binding  
489 mechanism of three sodium ions and aspartate in the glutamate transporter homologue  
490 GltTk. *Nat Commun* 7: 13420

491 Heinzelmann G, Kuyucak S (2014) Molecular dynamics simulations of the mammalian  
492 glutamate transporter EAAT3. *PLoS One* 9: e92089

493 Holley DC, Kavanaugh MP (2009) Interactions of alkali cations with glutamate  
494 transporters. *Philos Trans R Soc Lond B Biol Sci* 364: 155-161

495 Jensen AA, Erichsen MN, Nielsen CW, Stensbol TB, Kehler J, Bunch L (2009)  
496 Discovery of the first selective inhibitor of excitatory amino acid transporter subtype 1.  
497 *J Med Chem* 52: 912-915

498 Kabsch W (2010) Xds. *Acta Crystallogr D Biol Crystallogr* 66: 125-132

499 Kanner BI, Sharon I (1978) Active transport of L-glutamate by membrane vesicles  
500 isolated from rat brain. *Biochemistry* 17: 3949-3953

501 Kavanaugh MP, Bendahan A, Zerangue N, Zhang Y, Kanner BI (1997) Mutation of an  
502 amino acid residue influencing potassium coupling in the glutamate transporter GLT-1  
503 induces obligate exchange. *J Biol Chem* 272: 1703-1708

504 Koch HP, Larsson HP (2005) Small-scale molecular motions accomplish glutamate  
505 uptake in human glutamate transporters. *J Neurosci* 25: 1730-1736

506 Kortzak D, Alleva C, Weyand I, Ewers D, Zimmermann MI, Franzen A, Machtens JP,  
507 Fahlke C (2019) Allosteric gate modulation confers K(+) coupling in glutamate  
508 transporters. *EMBO J* 38: e101468

509 Larsson HP, Wang X, Lev B, Bacongus I, Caplan DA, Vyleta NP, Koch HP, Diez-  
510 Sampedro A, Noskov SY (2010) Evidence for a third sodium-binding site in glutamate  
511 transporters suggests an ion/substrate coupling model. *Proc Natl Acad Sci U S A* 107:  
512 13912-13917

513 Leary GP, Stone EF, Holley DC, Kavanaugh MP (2007) The glutamate and chloride  
514 permeation pathways are colocalized in individual neuronal glutamate transporter  
515 subunits. *J Neurosci* 27: 2938-2942

516 Lehre KP, Danbolt NC (1998) The number of glutamate transporter subtype molecules  
517 at glutamatergic synapses: chemical and stereological quantification in young adult rat  
518 brain. *J Neurosci* 18: 8751-8757

519 Mastrorarde DN (2005) Automated electron microscope tomography using robust  
520 prediction of specimen movements. *J Struct Biol* 152: 36-51

521 Matin TR, Heath GR, Huysmans GHM, Boudker O, Scheuring S (2020) Millisecond  
522 dynamics of an unlabeled amino acid transporter. *Nat Commun* 11: 5016

523 McCoy AJ, Grosse-Kunstleve RW, Adams PD, Winn MD, Storoni LC, Read RJ (2007)  
524 Phaser crystallographic software. *J Appl Crystallogr* 40: 658-674

525 Nayal M, Di Cera E (1996) Valence screening of water in protein crystals reveals  
526 potential Na<sup>+</sup> binding sites. *J Mol Biol* 256: 228-234

527 Nelson PJ, Dean GE, Aronson PS, Rudnick G (1983) Hydrogen ion cotransport by the  
528 renal brush border glutamate transporter. *Biochemistry* 22: 5459-5463

529 Pajarillo E, Rizer A, Lee J, Aschner M, Lee E (2019) The role of astrocytic glutamate  
530 transporters GLT-1 and GLAST in neurological disorders: Potential targets for  
531 neurotherapeutics. *Neuropharmacology* 161: 107559

532 Pettersen EF, Goddard TD, Huang CC, Couch GS, Greenblatt DM, Meng EC, Ferrin  
533 TE (2004) UCSF Chimera--a visualization system for exploratory research and  
534 analysis. *J Comput Chem* 25: 1605-1612

535 Punjani A, Rubinstein JL, Fleet DJ, Brubaker MA (2017) cryoSPARC: algorithms for  
536 rapid unsupervised cryo-EM structure determination. *Nat Methods* 14: 290-296

537 Punjani A, Zhang H, Fleet DJ (2020) Non-uniform refinement: adaptive regularization  
538 improves single-particle cryo-EM reconstruction. *Nat Methods* 17: 1214-1221

539 Qiu B, Matthies D, Fortea E, Yu Z, Boudker O (2021) Cryo-EM structures of excitatory  
540 amino acid transporter 3 visualize coupled substrate, sodium, and proton binding and  
541 transport. *Sci Adv* 7

542 Rey M, Sarpe V, Burns KM, Buse J, Baker CA, van Dijk M, Wordeman L, Bonvin  
543 AM, Schriemer DC (2014) Mass spec studio for integrative structural biology.  
544 *Structure* 22: 1538-1548

545 Reyes N, Ginter C, Boudker O (2009) Transport mechanism of a bacterial homologue  
546 of glutamate transporters. *Nature* 462: 880-885

547 Reyes N, Oh S, Boudker O (2013) Binding thermodynamics of a glutamate transporter  
548 homolog. *Nat Struct Mol Biol* 20: 634-640

549 Ruan Y, Miyagi A, Wang X, Chami M, Boudker O, Scheuring S (2017) Direct  
550 visualization of glutamate transporter elevator mechanism by high-speed AFM. *Proc*  
551 *Natl Acad Sci U S A* 114: 1584-1588

552 Ryan RM, Compton EL, Mindell JA (2009) Functional characterization of a Na<sup>+</sup>-  
553 dependent aspartate transporter from *Pyrococcus horikoshii*. *J Biol Chem* 284: 17540-  
554 17548

555 Seal RP, Amara SG (1998) A reentrant loop domain in the glutamate carrier EAAT1  
556 participates in substrate binding and translocation. *Neuron* 21: 1487-1498

557 Tao Z, Rosental N, Kanner BI, Gameiro A, Mwaura J, Grewer C (2010) Mechanism of  
558 cation binding to the glutamate transporter EAAC1 probed with mutation of the  
559 conserved amino acid residue Thr101. *J Biol Chem* 285: 17725-17733

560 Thorn A, Sheldrick GM (2011) ANODE: anomalous and heavy-atom density  
561 calculation. *J Appl Crystallogr* 44: 1285-1287

562 Verdon G, Oh S, Serio RN, Boudker O (2014) Coupled ion binding and structural  
563 transitions along the transport cycle of glutamate transporters. *Elife* 3: e02283

564 Wang H, Rascoe AM, Holley DC, Gouaux E, Kavanaugh MP (2013) Novel  
565 dicarboxylate selectivity in an insect glutamate transporter homolog. *PLoS One* 8:  
566 e70947

567 Wang J, Zhang K, Goyal P, Grewer C (2020) Mechanism and potential sites of  
568 potassium interaction with glutamate transporters. *J Gen Physiol* 152

569 Watzke N, Rauen T, Bamberg E, Grewer C (2000) On the mechanism of proton  
570 transport by the neuronal excitatory amino acid carrier 1. *J Gen Physiol* 116: 609-622  
571 Yernool D, Boudker O, Folta-Stogniew E, Gouaux E (2003) Trimeric subunit  
572 stoichiometry of the glutamate transporters from *Bacillus caldotenax* and *Bacillus*  
573 *stearothermophilus*. *Biochemistry* 42: 12981-12988  
574 Yernool D, Boudker O, Jin Y, Gouaux E (2004) Structure of a glutamate transporter  
575 homologue from *Pyrococcus horikoshii*. *Nature* 431: 811-818  
576 Zerangue N, Kavanaugh MP (1996) Flux coupling in a neuronal glutamate transporter.  
577 *Nature* 383: 634-637  
578 Zhang Y, Bendahan A, Zerbiv R, Kavanaugh MP, Kanner BI (1998) Molecular  
579 determinant of ion selectivity of a (Na<sup>+</sup> + K<sup>+</sup>)-coupled rat brain glutamate transporter.  
580 *Proc Natl Acad Sci U S A* 95: 751-755  
581 Zhou Y, Danbolt NC (2014) Glutamate as a neurotransmitter in the healthy brain. *J*  
582 *Neural Transm (Vienna)* 121: 799-817  
583



584 **Methods**

585 **Protein expression and purification**

586 Genes encoding EAAT1 and thermostabilized EAAT1<sub>CRYST</sub> constructs were cloned  
587 into the pcDNA3.1(+) plasmid (Invitrogen) as previously described with N-terminal  
588 Strep-tag II affinity tag, eGFP and PreScission site(Canul-Tec *et al.*, 2017). Protein was  
589 expressed in HEK293F cells (Thermo Fisher Scientific) grown in Freestyle293 medium  
590 (Invitrogen) at 37 °C to densities of  $2.5 \times 10^6$  cells ml<sup>-1</sup>. Cells were transiently  
591 transfected using 7.5 mg ml<sup>-1</sup> polyethylenimine (PEI) (Polysciences) and 2.5 mg ml<sup>-1</sup>  
592 of DNA. Transfected cells were diluted with an equivalent volume of Freestyle293  
593 medium 8 h post-transfection and treated with 10 mM of sodium butyrate (Sigma) 12  
594 h after dilution. Cells were harvested by centrifugation 48 h after transfection,  
595 resuspended at 1:4 (w/v) ratio in cold buffer containing 50 mM HEPES/Tris-base, pH  
596 7.4, 50 mM NaCl, 1 mM L-asp, 1 mM EDTA, 1 mM Tris(2-carboxyethyl) phosphine  
597 (TCEP), 1 mM Phenylmethylsulfonyl fluoride (PMSF) and 1:200 (v/v) dilution of  
598 mammalian protease inhibitor cocktail (Sigma), and flash-frozen in liquid nitrogen for  
599 storage at -80 °C.

600 Cell suspension was thawed and diluted 1:2 volumes in buffer complemented with 350  
601 mM NaCl, 10% glycerol, 1% dodecanoyl sucrose (DDS, Anatrace) and 0.2%  
602 Cholesteryl Hemisuccinate Tris Salt (CHS, Anatrace). After 1 h detergent extraction,  
603 cell debris was removed (4,500 g, 0.5 h), and the supernatant cleared (186,000 g for 1  
604 h). Clear lysate was incubated with Strep-Tactin Sepharose High Performance resin  
605 (GE Healthcare) previously equilibrated with buffer containing 50 mM HEPES/Tris-  
606 base, pH 7.4, 200 mM NaCl, 1 mM L-asp, 1 mM TCEP, 5% glycerol, 0.05% DDS and  
607 0.01% CHS, for 2 h. In crystallization experiments of apo transporters in Rb<sup>+</sup> or choline  
608 buffers (see below) resin incubation was preceded by an ultracentrifugation membrane-

609 wash step, as described before (Canul-Tec *et al.*, 2017). Resin was washed with 20  
610 column volumes (CV) of equilibration buffer supplemented with 1:1:1 lipid mixture of  
611 1-palmitoyl-2-oleoyl-sn-glycero-3-phosphocholine (POPC), 1-palmitoyl-2-oleoyl-sn-  
612 glycero-3-phosphoethanolamine (POPE) and 1-palmitoyl-2-oleoyl-sn-glycero-3-  
613 phosphoglycerol (POPG) (Avanti Polar Lipids) at total concentration of 25  $\mu$ M. Protein  
614 was eluted with buffer supplemented with 2.5 mM D-desthiobiotin (Sigma), and  
615 subjected to N-term PreScission cleavage during 2 h. The sample was concentrated with  
616 100-kDa cutoff Amicon centrifugal filter unit (Millipore) and injected into a size-  
617 exclusion chromatography (SEC) column Superose 6 10/300 (GE Healthcare),  
618 equilibrated in different buffers (see below). All purification steps were carried out at  
619 4 °C.

#### 620 **Intrinsic-tryptophan fluorescence binding assay**

621 PreScission-treated EAAT1<sub>CRYST</sub> and mutant transporters were further purified by SEC  
622 in buffer containing: HEPES/Tris-base, pH 7.4, 200 mM NaCl, 1 mM L-asp, 1 mM  
623 TCEP, 5% glycerol, 0.05% DDS, 0.01% CHS and 25  $\mu$ M lipid mix. Peak fractions were  
624 concentrated using a 100-kDa cutoff Amicon centrifugal filter, and then diluted 10-fold  
625 in buffer: 50 mM HEPES/Tris-base, pH 7.4, 200 mM ChCl, 1 mM TCEP, 0.05% DDS  
626 and 0.01% CHS. This procedure was repeated three times to ensure buffer exchange.  
627 Binding experiments started by further diluting transporters ~ 100-fold in a 1-ml quartz  
628 cuvette filled with the above-mentioned Ch<sup>+</sup>-based buffer to reach 2-4  $\mu$ M final  
629 protomer concentration. In L-asp titrations, final NaCl or CaCl<sub>2</sub> concentrations were  
630 added to the cuvette as indicated in the Figures. To assay binding of ligands in the  
631 presence of UCPH<sub>101</sub>, 20  $\mu$ M final concentration was added to both protein sample and  
632 cuvette, and allowed for ~30 min equilibration time. Binding experiments at different

633 pH values were done by substituting HEPES/tris-base with MES/tris-base (pH 5 and  
634 6), or Tris/HCl (pH 9 and 10) in the cuvette buffer.

635 Experiments were done at 25 °C under stirring. Intrinsic tryptophan fluorescence was  
636 excited at 280 nm, and emission recorded at 325 nm using a QuantaMaster 40  
637 spectrofluorometer (Horiba). Protein samples were equilibrated for 2-min in the  
638 cuvette, before ligand addition at different concentrations, and fluorescence emission  
639 was averaged over the last 10s after equilibration. Fractional fluorescence changes were  
640 fitted to the Hill equation. Data analysis, fitting, and figures were done with SigmaPlot  
641 12 (Systat Software, Inc).

#### 642 **Crystallization and structure determination**

643 PreScission-treated transporters were supplemented with 100  $\mu$ M UCPH<sub>101</sub> (Abcam)  
644 for 30 minutes at 4 °C, and further purified by SEC in buffers at pH 7.4 (HEPES/Tris-  
645 base), containing 1 mM TCEP, 5% glycerol, 100  $\mu$ M UCPH<sub>101</sub>, 0.25% decanoyl  
646 sucrose (DS, Merck Millipore), 0.05% CHS, 25  $\mu$ M lipid mix, and one of the following:  
647 200 mM Na and 1 mM L-asp (Na<sup>+</sup>/asp-bound state); 200 mM RbCl (Rb<sup>+</sup>/Ba<sup>2+</sup>-bound  
648 state); or 200 mM ChCl (Ba<sup>2+</sup>-bound state). Peak fractions were concentrated to 4 mg  
649 ml<sup>-1</sup>, supplemented with 0.2% n-Octyl-b-D-glucopyranoside (BOG, Anatrace) and  
650 0.04% CHS, and used immediately for crystallization. Vapor-diffusion hanging-drop  
651 crystallization and cryogenic conditions were as previously described (Canul-Tec *et al.*,  
652 2017), using equal volumes of sample and a reservoir solution containing 100 mM Tris,  
653 pH 8.2, 28-32% (v/v) PEG 400, 50 mM CaCl<sub>2</sub> and 50 mM BaCl<sub>2</sub>.

654 Complete and highly-redundant X-ray diffraction datasets were collected at tunable  
655 beamlines PROXIMA-1 (SOLEIL synchrotron, St. Aubin, France), as well as ID29 and  
656 ID30B (European Synchrotron Radiation Facility, Grenoble, France). EAAT1<sub>CRSYT</sub> and  
657 EAAT1<sub>CRYST-II</sub> crystals purified in Rb<sup>+</sup>- or Ch<sup>+</sup>-based buffers were smaller and typically

658 diffracted at significant lower resolutions ( $> 6\text{\AA}$ ) than those purified in  $\text{Na}^+$ /asp-based  
659 buffers ( $< 4\text{\AA}$ ), and they required larger crystal-screening efforts to collect datasets at  
660 the reported resolutions.

661 Diffraction datasets were processed as described before (Canul-Tec *et al.*, 2017) using  
662 XDS package (Kabsch, 2010) and AIMLESS (Evans & Murshudov, 2013). All crystals  
663 belonged to the same space group ( $P6_3$ ), and diffracted anisotropically. Anisotropy  
664 correction was made with STARANISO (Global Phasing Lim.). Appendix Table S1  
665 and S2 include comparison of reflection statistics before and after anisotropic  
666 correction reflecting complete sampling of reciprocal space, as well as refinement  
667 statistics of reflections along crystallographic axes. Corrected anisotropic amplitudes  
668 were used for molecular replacement in PHASER (McCoy *et al.*, 2007), using TranD  
669 and ScaD of EAAT1<sub>CRYST</sub> or EAAT1<sub>CRYST-II</sub> (PDB codes 5LLM and 5LM4,  
670 respectively) as independent search models. Final electron density maps were obtained  
671 through rounds of manual building in COOT (Emsley *et al.*, 2010) and refinement in  
672 Buster (Blanc *et al.*, 2004), until reaching good crystallographic statistics and  
673 stereochemistry (Appendix Table S1 and S2). Anomalous difference maps were  
674 calculated with SHELX and ANODE (Thorn & Sheldrick, 2011) using diffraction data  
675 with high-resolution cutoff of  $6\text{\AA}$ , and without anisotropic correction.

676 In the  $\text{Na}^+$ /asp-bound EAAT1<sub>CRYST</sub> structure, we modelled extra electron density in the  
677 tranD (TM7-HP2 loop, residues 397-403), and in the scaD N-terminus (TM1a' helix,  
678 residues 26-36). Rounds of refinement with extended transporter models incrementally  
679 improved the quality of 2Fo-Fc maps, and yielded three peaks in the Fo-Fc omit maps  
680 that localize to conserved Na1-Na3. We modelled 3  $\text{Na}^+$  bound to the transporter at  
681 these peaks. We also calculated anomalous differences maps, and observed a single  
682 anomalous peak on the surface of the ScaD, nearby residue Q245 (TM5), that we

683 modeled as a bound barium ion with low occupancy (0.35). Our functional and  
684 structural data do not support functional roles of this ion on the transport mechanism.  
685 Rb<sup>+</sup>/Ba<sup>2+</sup> and Ba<sup>2+</sup> bound electron density maps of apo transporters, respectively, were  
686 lower resolution compared to Na<sup>+</sup>/asp-bound. This is likely due to the observed  
687 conformational re-arrangements of the tranD that break or weaken crystal-lattice  
688 contacts between TM1a' and extracellular tranD surface of a crystallographic-  
689 symmetry mate. Consistently, in Rb<sup>+</sup>/Ba<sup>2+</sup> and Ba<sup>2+</sup> bound structures, respectively,  
690 TM7-HP2 loop and TM1a' were not modeled due to lack of density in these regions.  
691 Rb<sup>+</sup> at K<sub>CT</sub>, as well as Ba<sup>2+</sup> at Na3 were modeled based on anomalous difference maps  
692 from datasets at maximum and off-maximum Rb<sup>+</sup> absorption wavelengths,  
693 respectively.

694 Atomic model validation was performed with Molprobit (Chen *et al*, 2010). Structural  
695 figures were prepared with PyMOL Molecular Graphics System (Schrodinger, LLC).

#### 696 **Cryo-EM sample preparation, data collection and processing**

697 EAAT1<sub>WT</sub> (Uniprot P43003) sequence was mutated at predicted N-glycosylation sites  
698 (N206T, and N216T), and expressed and purified as mentioned above, with SEC buffer  
699 containing: 50 mM HEPES/Tris-base, pH 7.4, 100 mM KCl, 1 mM TCEP, 0.0084%  
700 glycol-diosgenin (GDN), and 0.0017% CHS. Peak fractions were concentrated at 4-5  
701 mg ml<sup>-1</sup> and spotted immediately on glow-discharged Quantifoil R1.2/1.3 Au grids  
702 (Quantifoil Micro Tools GmbH), and plunge frozen using a Vitrobot Mark IV (FEI) at  
703 4°C under 100% humidity. Grids were stored in liquid nitrogen.

704 Cryo-EM micrographs were recorded on a Titan Krios electron microscope (Thermo  
705 Fisher Scientific) operated at 300 kV, equipped with GatanK2 direct electron detector  
706 (Appendix Table S3). Movies were collected on counting mode automatically using  
707 SerialEM (Mastrorade, 2005) with a pixel size of 0.814 Å. The defocus range was -

708 0.8 to -2.0  $\mu\text{m}$  and each movie contained 40 frames with a dose per frame of 1.03  
709 electrons/ $\text{\AA}^2$ , and total exposure time 8 s.

710 Single-particle data processing was done in cryoSPARCv3.1.0 (Punjani *et al.*, 2017)  
711 (Appendix Figure S3). Beam-induced patch-motion correction, and patch contrast  
712 transfer function estimation were done with in-built cryoSPARC routines, respectively.

713 2,298,481 auto-picked particles were 2x binned and extracted from 13,607 manually-  
714 selected movies. Initially, 517,319 selected from 2D-classification were subjected to  
715 several rounds of *ab initio* classification. This yielded a 3D reconstruction from 71,296  
716 particles in which the transmembrane helices of the transporter were evident, but  
717 refined at  $> 6 \text{ \AA}$  using unbinned particles for non-uniform refinement (Punjani *et al.*,  
718 2020). We then input those *ab initio* volumes to re-classify the original set of 2,298,481  
719 2x-binned particles using several rounds of heterogenous refinement. In the first round  
720 of heterogenous refinement, two unrelated cryo-EM maps were included as templates  
721 to aid discarding bad particles. From this, 433,972 particles were selected and unbinned  
722 for further rounds of heterogenous refinement and *ab initio* classification. An *ab initio*  
723 3D reconstruction from a final set of 34,433 particles yielded a map at an overall  $\sim 4.0$   
724  $\text{\AA}$ , after non-uniform refinement with C3 symmetry imposed. The map quality was  
725 significantly better in the region corresponding to the scaD than that of the tranD. This  
726 is somehow expected, since the three tranDs undergo independent conformational  
727 changes both relative to the three scaDs, as well as locally.

728 For model building, the scaD and tranD of  $\text{Rb}^+/\text{Ba}^{2+}$  bound X-ray structure were fitted  
729 into the EM map as separate rigid-bodies using Chimera. This initial model was then  
730 adjusted manually in COOT preserving the secondary structure observed in the crystal.

731 We also used the cryoEM structure of ASCT2 (PDB 6GCT) (Garaeva *et al.*, 2018) as  
732 a reference for regions of the tranD that were not modeled in the crystal structure and

733 for which we had density in the cryo-EM map. We omitted conserved residues  
734 <sup>398</sup>NMD<sup>400</sup> in the final cryo-EM model due to lack of density in this region. The final  
735 model was refined in PHENIX (Adams *et al*, 2010), and figures made with UCSF  
736 Chimera (Pettersen *et al*, 2004), UCSF ChimeraX (Goddard *et al*, 2018), and PYMOL.

### 737 **Radioactive substrate transport assays**

738 Liposomes were formed at 5:1 molar ratio of POPC and Cholesteryl Hemisuccinate  
739 (Avanti Polar Lipids) and resuspended at 8 mg ml<sup>-1</sup> in buffer containing 50 mM  
740 HEPES/Tris, pH 7.4 and 200 mM NaCl, and pre-treated with 1.3% DDS and 0.26%  
741 CHS for 1 h. eGFP-EAAT1<sub>CRYST</sub> fusion construct was purified by SEC in buffer  
742 containing: HEPES/Tris-base, pH 7.4, 200 mM NaCl, 1 mM L-asp, 1 mM TCEP, 5%  
743 glycerol, 0.05% DDS, 0.01% CHS and 25 μM lipid mix. Purified eGFP-EAAT1<sub>Cryst</sub>  
744 was mixed with destabilized liposomes at a 1:40 (w/w, protein/lipid ratio) for 1 h.  
745 Detergent removal was repeated three times with Biobeads SM-2 (BioRad) at 100 mg  
746 ml<sup>-1</sup> and at 4 °C. Proteoliposomes were loaded with internal buffer (50 mM  
747 HEPES/Tris-base, pH 7.4 buffer, 200 mM KCl and 1.25% glycerol) through 10 freeze-  
748 thaw cycles followed by 10 extrusion cycles through 400-nm polycarbonate  
749 membranes (Avanti Polar Lipids). Proteoliposomes were centrifuged (164,300 g, 30  
750 min at 4 °C) and resuspended at 100 mg of lipids ml<sup>-1</sup> in buffer containing 50 mM  
751 HEPES/Tris-base, pH 7.4, 200 mM choline chloride (ChCl) and 1.25% glycerol for  
752 immediate use.

753 Substrate uptake was performed at 37°C for 30 min, and initiated by diluting  
754 proteoliposomes 10-fold into buffer containing 50 mM HEPES/Tris-base, pH 7.4, 200  
755 mM NaCl, 1.25% glycerol, 50 μM L-glutamate and 10 μM L-[<sup>14</sup>C(U)]-glutamate  
756 (PerkingElmer). Uptake was stopped with 5-fold dilution of proteo-liposome mix into  
757 ice-cold buffer (50 mM HEPES/Tris-base, pH 7.4, 200 mM ChCl and 1.25% glycerol)

758 followed by immediate filtration and wash on nitrocellulose 0.22- $\mu$ m filters (Merck  
759 Millipore). Background radioactivity was estimated on each sample using  
760 proteoliposomes diluted in buffer containing 200 mM ChCl, instead of NaCl, and  
761 subtracted during analysis. Filter membranes were transferred to scintillation cocktail  
762 Ultima Gold (PerkinElmer), and radioactivity quantified using Tri-Carb 3110TR  
763 counter (PerkinElmer). This setup was used to calibrate different batches of radioactive  
764 L-glutamate source. Protein quantification was done in an Infinite M1000Pro  
765 microplate reader (Tecan) using calibrated eGFP fluorescence intensity.

766 Uptake experiments at different pH values were done with modified external buffers  
767 containing: 50 mM MES/Tris-base pH 6.0, HEPES/Tris-base pH 7.4, or 50 mM  
768 Tris/HCl pH 9.0 or 10.0. Counter-transported ions were probed by exchanging KCl in  
769 the intraliposomal buffer for equal concentrations of RbCl, or ChCl, or 125 mM ChCl  
770 and 50 mM CaCl<sub>2</sub> through freezing-thawing cycles. Reported values are means of at  
771 least three independent experiments, each one measured at least in triplicates.

772 In HEK293-cells uptake experiments, cells were collected 36-44 h after transfection,  
773 washed two times, and resuspended at a density of  $50 \times 10^6$  cells ml<sup>-1</sup> in buffer 11 mM  
774 HEPES/Tris-base, pH 7.4, 140 mM ChCl, 4.7 mM KCl, 2.5 mM CaCl<sub>2</sub>, 1.2 mM MgCl<sub>2</sub>,  
775 and 10 mM D-glucose, for immediate use. Substrate uptake was performed as described  
776 in liposomes with some variations. For experiments shown in Appendix Figure 1,  
777 reaction time was 1 min in buffer containing 11 mM HEPES/Tris-base, pH 7.4, 140  
778 mM NaCl, 4.7 mM KCl, 2.5 mM CaCl<sub>2</sub>, 1.2 mM MgCl<sub>2</sub>, 10 mM D-glucose, 50  $\mu$ M L-  
779 glutamate, and 5  $\mu$ M [<sup>14</sup>C] L-glutamate. For experiments shown in Fig. EV5, reaction  
780 time was 15 min in buffer containing 11 mM HEPES/Tris-base, pH 7.4, 140 mM NaCl,  
781 4.7 mM KCl, 5 mM CaCl<sub>2</sub>, 10 mM D-glucose, and either 50  $\mu$ M L-glutamate/10  $\mu$ M



782 [<sup>14</sup>C] L-glutamate, or 15 μM L-glutamate/5 μM [<sup>14</sup>C] L-glutamate. In Mg<sup>2+</sup>-containing  
783 conditions, all Ca<sup>2+</sup> was substituted for Mg<sup>2+</sup>.

784 Cells were filtered using 0.8-μm nitrocellulose filters, and background radioactivity  
785 was estimated from cells transfected with empty vector in NaCl reaction buffer, and  
786 subtracted from the uptake data. Reported values are means of three independent  
787 experiments measured in duplicates.

### 788 **Hydrogen-deuterium exchange mass spectrometry (HDX-MS)**

789 PreScission-treated EAAT1<sub>CRYST</sub> was further purified by SEC in buffer containing:  
790 HEPES/Tris-base, pH 7.4, 200 mM NaCl, 1 mM L-asp, 1 mM TCEP, 5% glycerol,  
791 0.05% DDS, 0.01% CHS, 25 μM lipid mix, and 100 μM UCPH<sub>101</sub>. This sample  
792 constitutes reference Na<sup>+</sup>/L-asp-bound state. K<sup>+</sup>-bound state was obtained by two  
793 cycles of 10-fold dilution-concentration of reference samples in buffer: 50 mM  
794 HEPES/Tris-base, pH 7.4, 200 mM KCl, 1 mM TCEP, 100 μM UCPH<sub>101</sub>, 0.05% DDS  
795 and 0.01% CHS. To probe reversibility of K<sup>+</sup>-induced HDX changes, a Na<sup>+</sup>/L-asp-  
796 bound control state was generated by addition of 200 mM NaCl and 1 mM L-asp to the  
797 K<sup>+</sup>-bound state. Final concentration of all samples for HDX-MS analysis was ~0.8 mg  
798 ml<sup>-1</sup>.

799 Peptide map was generated using nanoLC-MS/MS. 20 pmol of reference transporters  
800 were digested for 2min in 0.75% formic acid using an immobilized pepsin column (2.1  
801 x 20 mm, Affipro). Peptic peptides were collected and purified onto C18 Stage-Tips  
802 before nanoLC-MS/MS analysis using an EASY-nLC<sup>TM</sup> 1200 system (Thermo-  
803 Scientific) coupled to the nanoelectrospray ion source of an Orbitrap Q-Exactive Plus  
804 mass spectrometer (Thermo-Scientific). Peptides were loaded on an in-house packed  
805 nano-HPLC column (75 μm x 25 cm) with C18 resin (Aeris PEPTIDE XB-C18, 1.7μm  
806 particles, 100 Å pore size, Phenomenex) and separated by reverse-phase

807 chromatography at 250 nL/min using a gradient of acetonitrile with 0.1% formic acid.  
808 The Orbitrap mass spectrometer was set up in data-dependent acquisition mode. After  
809 a survey scan in the Orbitrap (resolution 60,000 at  $m/z$  400), the 10 most intense  
810 precursor ions were selected for HCD fragmentation with a normalized collision energy  
811 set up to 28 (resolution 30,000). Only charge states between 1 and 10 were selected and  
812 a dynamic exclusion of 20 s was set. NanoLC-MS/MS data were processed  
813 automatically using Mass Spec Studio v1.3.2(Rey *et al*, 2014) to identify peptides with  
814 the following parameters: 4-40 amino acid length, charge states between 1 and 5, mass  
815 accuracy of 7 ppm for both MS and MS/MS, and a false discovery rate (FDR) of 5%.  
816 Deuterium exchange was initiated by diluting 64 pmol of purified transporter with the  
817 appropriate labeling buffers at 25°C. These buffers reached final level of 80% D<sub>2</sub>O and  
818 otherwise were as described above for reference, K<sup>+</sup>-bound and control states,  
819 respectively. 30 pmol transporter aliquots were removed at 60s, and immediately  
820 quenched with a cold acidic solution (1.25% formic acid) to decrease the pH to 2.5.  
821 Samples were then snap-frozen in liquid nitrogen and stored at -80°C until LC-MS  
822 analysis.  
823 Quenched samples were rapidly thawed and injected into a cooled ACQUITY UPLC  
824 M-Class HDX system (Waters) maintained at 4°C. 15 pmol of transporter were online  
825 digested for 3 min at 20°C and 80  $\mu$ L/min of solvent A (0.15% formic acid (v/v) in  
826 water) using an immobilized pepsin column (2.1 x 20 mm, Affipro). Peptic peptides  
827 were desalted onto a C18 trap column (Kinetex® EVO C18, 2.6 $\mu$ m, 100Å, 2.1 x 20  
828 mm, Phenomenex) at a flow rate of 80  $\mu$ L/min of solvent A and then separated at 70  
829  $\mu$ L/min by a linear gradient from 10 to 60% of solvent B (0.15% formic acid (v/v) in  
830 acetonitrile) in 11 min using a C18 analytical column (Kinetex® EVO C18, 1.7 $\mu$ m,  
831 100Å, 1 x 100 mm, Phenomenex). The pepsin column was washed with 1.5M

832 guanidinium chloride / 5% acetonitrile / 1% formic acid. Blank injections were  
833 performed between each run to ensure the absence of carry-over. The LC flow was  
834 directed to a Synapt™ G2-Si HDMS™ mass spectrometer (Waters) equipped with an  
835 electrospray ionization (ESI) source. Mass spectra were acquired in positive and  
836 resolution mode over the m/z range of 300-1500 with 0.5 s scan time.

837 Data analysis was performed on biological triplicates using at least five replicates per  
838 transporter state. Deuterium uptake values were calculated for each peptide using Mass  
839 Spec Studio v1.3.2 and no adjustment was made for back-exchange. Student t-tests and  
840 Woods plots were performed for each transporter state using the embedded statistical  
841 module in Mass Spec Studio v1.3.2 with the following parameters: standard deviation  
842 cutoff = 2 and 1-p cutoff = 0.99.

#### 843 **Data availability**

844 Atomic coordinates of crystal structures were deposited in the RCSB Protein Data Bank  
845 (PDB) under the following accession numbers: Na<sup>+</sup>/transmitter bound EAAT1<sub>CRYST</sub>  
846 (7AWM; <https://doi.org/10.2210/pdb7AWM/pdb>); Na<sup>+</sup>/transmitter bound  
847 EAAT1<sub>CRYST</sub>-E386Q (7AWQ; <https://doi.org/10.2210/pdb7AWQ/pdb>); Rb<sup>+</sup>/Ba<sup>2+</sup>  
848 bound EAAT1<sub>CRYST</sub> (7AWN; <https://doi.org/10.2210/pdb7AWN/pdb>); Rb<sup>+</sup>/Ba<sup>2+</sup>  
849 bound EAAT1<sub>CRYST-II</sub> (7AWP; <https://doi.org/10.2210/pdb7AWP/pdb>); and Ba<sup>2+</sup>  
850 bound EAAT1<sub>CRYST-II</sub> (7AWL; <https://doi.org/10.2210/pdb7AWL/pdb>). Atomic  
851 coordinates and cryo-EM map of EAAT1<sub>WT</sub> structure were deposited in the PDB  
852 (7NPW; <https://doi.org/10.2210/pdb7NPW/pdb>), and Electron Microscopy Data Bank  
853 (EMD-12524; <https://www.emdataresource.org/EMD-12524>).

#### 854 **Code availability**

855 In-house script to facilitate reflection processing with STARANISO (P.L.) is available  
856 at

857 ([https://raw.githubusercontent.com/legrandp/xdsme/master/bin/noarch/run\\_xds2staran](https://raw.githubusercontent.com/legrandp/xdsme/master/bin/noarch/run_xds2staran)  
858 [iso.sh](#))

859

## 860 **Acknowledgements**

861 We thank Ahmed Haouz and the staff at the crystallography core facility of the Institut  
862 Pasteur for assistance with crystallization screens; Staff at Synchrotron Soleil and the  
863 European Synchrotron Radiation Facility for assistance with data collection; The IECB  
864 cryoEM imaging facility is acknowledged for support in cryo-EM sample screening  
865 and initial data acquisition; the EMBL-Heidelberg Cryo-Electron Microscopy Service  
866 Platform for support in cryoEM data collection. The work was funded by the European  
867 Research Council (ERC grant 309657 to N.R.). J.C.C-T was partly supported by a  
868 Pasteur-Roux Postdoctoral Fellowship. Further support from Institut Pasteur, INCA  
869 2017-44 Grant, CACSICE grant (ANR-11-EQPX-008), and CNRS UMR3528 to N.R.  
870 and J.C.-R. is acknowledged.

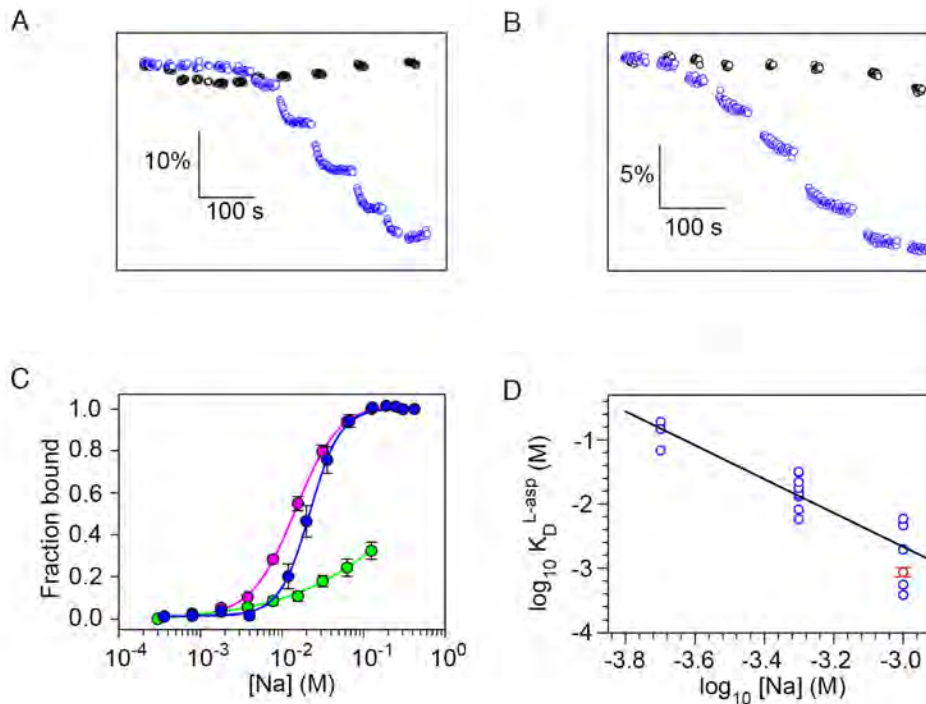
## 871 **Author contribution**

872 J.C.C.-T. optimized and performed protein expression, purification, and  
873 crystallization, as well as binding and transport assays; A.K. prepared and optimized  
874 cryo-EM grids and collected cryo-EM data. A.K and N.R. analyzed cryo-EM data  
875 and built the structure. R.A. performed molecular biology and uptake experiments  
876 in cells; J.C.C.-T and N.R. designed binding and uptake experiments, and analyzed  
877 those data; J.D. performed and analyzed HDX-MS experiments; M.R. and J.C.-R.  
878 designed and analyzed HDX-MS experiments.; J.C.C.-T. collected crystallographic  
879 data; J.C.C.-T., P.L., and N.R. analyzed diffraction data; J.C.C.-T and N.R.  
880 analyzed structures and prepared the manuscript, with contributions and edits

881 related to HDX from J.D., M.R., and J.C.-R., and those related to X-ray

882 crystallography from P.L.; N.R. conceived and supervised the project.

883



884

885

886 **Figure 1 Na<sup>+</sup> and transmitter binding**

887 A. Tryptophan-fluorescence time course associated to Na<sup>+</sup> (blue) and K<sup>+</sup> (black)  
 888 binding, respectively, to detergent-purified apo EAAT1<sub>CRYST</sub> at pH 7.4. Horizontal and  
 889 vertical scale bars represent time and  $\Delta F/F_0$ , respectively.

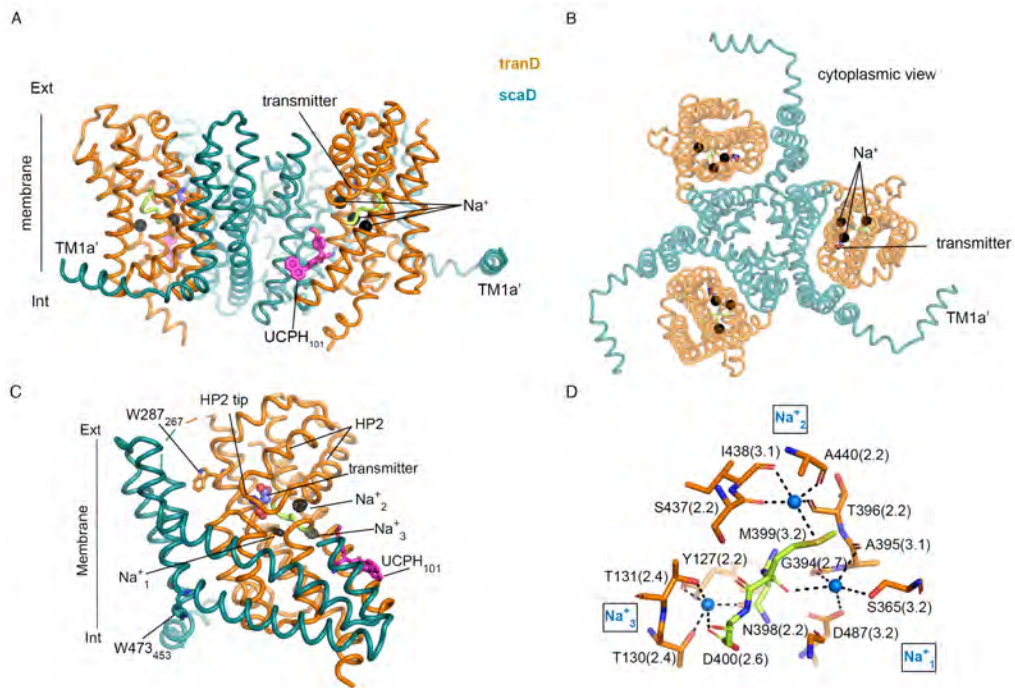
890 B. Tryptophan-fluorescence time course associated to L-asp binding in presence of 1  
 891 mM (blue) and absence (black) of Na<sup>+</sup>, respectively, at pH 9.

892 C. Na<sup>+</sup> binding isotherms of EAAT1<sub>CRYST</sub> at pH 7.4 in the presence (pink) and absence  
 893 (blue) of UPCH<sub>101</sub>. Mutation D400<sub>380</sub>N at Na3 strongly impairs Na<sup>+</sup> binding (green).  
 894 Solid lines represent fits of Hill equation.

895 D. Log-log plot of L-asp K<sub>D</sub> as a function of Na<sup>+</sup> concentration. Empty circles are K<sub>D</sub>  
 896 values (n=20) at pH=9.0 in the absence of UCPH<sub>101</sub> (blue), and solid line is the fit of a  
 897 straight line. For comparison, average L-asp K<sub>D</sub> at 1 mM Na<sup>+</sup> in the presence pf of  
 898 UPCH<sub>101</sub> is also shown (n=3; red).

899 Data information: in (C) symbols represent average and s.e.m. values of at least three  
 900 independent titrations. In (D), blue symbols represent individual K<sub>D</sub> values from n  
 901 number of independent titrations, and red symbol represents average and s.e.m values  
 902 from three experiments.

903



904

905

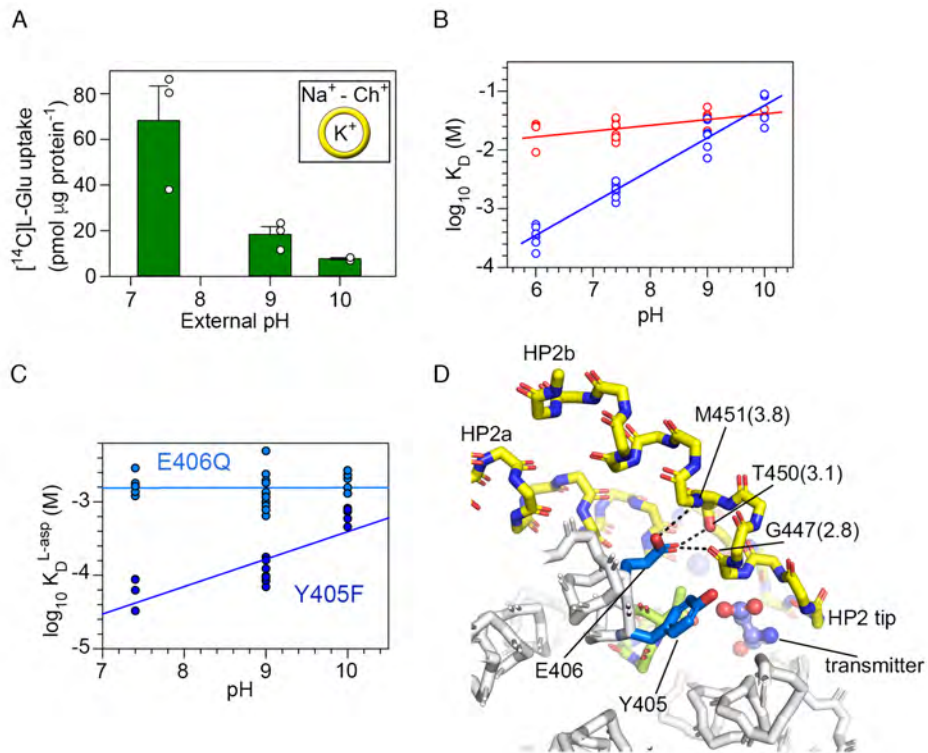
906 **Figure 2 EAAT1<sub>CRYST</sub> Na<sup>+</sup>/transmitter bound structure**

907 A, B. Views of EAAT1<sub>CRYST</sub> trimer in outward-facing Na<sup>+</sup>/transmitter-bound state,  
908 including N-term helix TM1a'.

909 C. EAAT1<sub>CRYST</sub> protomer viewed from the membrane with tranD orange, scaD teal  
910 (TM4a,b omitted), and <sup>398</sup>NMDG motif green. Fo-Fc Na<sup>+</sup>-omit map contoured at 3.5σ  
911 (black mesh) around the tranD core.

912 D. Coordination details of three Na<sup>+</sup>-bound (blue sphere) to EAAT1<sub>CRYST</sub>. Residue  
913 numbering corresponds to EAAT1<sub>WT</sub>, and the coordination distance (angstrom) is in  
914 parenthesis.

915



916

917

### Figure 3 H<sup>+</sup> and transmitter binding

918 A. Na<sup>+</sup>-induced L-glutamate uptake by purified EAAT1<sub>CRYST</sub> reconstituted in  
 919 liposomes loaded with K<sup>+</sup>. Choline (Ch<sup>+</sup>) condition was subtracted to the Na<sup>+</sup> condition.

920 B. Log-log plots of Na<sup>+</sup> (red, n=19) and L-asp (blue, n=27) K<sub>D</sub>, as a function of pH at  
 921 [Na<sup>+</sup>]=0.5 mM. Na<sup>+</sup> (n=10) and L-asp (n=7) titration data at pH 7.4 and 9.0,  
 922 respectively, are also reported in Fig. 1. Solid lines are fits of straight lines.

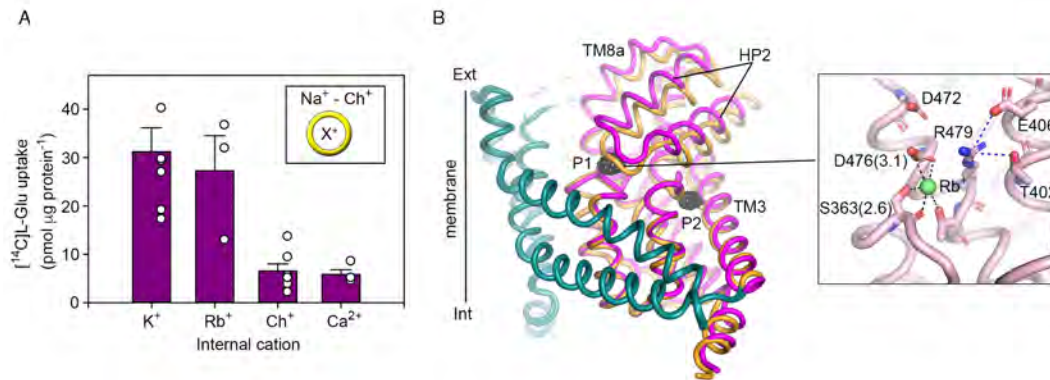
923 C. Log-log plots of L-asp K<sub>D</sub> for EAAT1<sub>CRYST</sub>-E406<sub>386</sub>Q (light blue, n=24) and  
 924 EAAT1<sub>CRYST</sub>-Y405<sub>385</sub>F (dark blue, n=18), as a function of pH at [Na<sup>+</sup>]=0.5 mM..

925 D. Potential H<sup>+</sup>-bond network between protonated E406<sub>386</sub> (TM7b) and residues in  
 926 HP2b in EAAT1<sub>CRYST</sub> transmitter-bound structure. HP2 is depicted in yellow and the  
 927 <sup>398</sup>NMDG motif in green. Residue numbering corresponds to EAAT1<sub>WT</sub>, and the  
 928 interatomic distance (angstrom) is parenthesis.

929 Data information: in (A) bar plots depict averages and s.e.m. values of three  
 930 independent experiments (empty circles) performed in triplicate. In (B,C) symbols  
 931 represent individual K<sub>D</sub> values from *n* number of independent titrations.

932





933

934

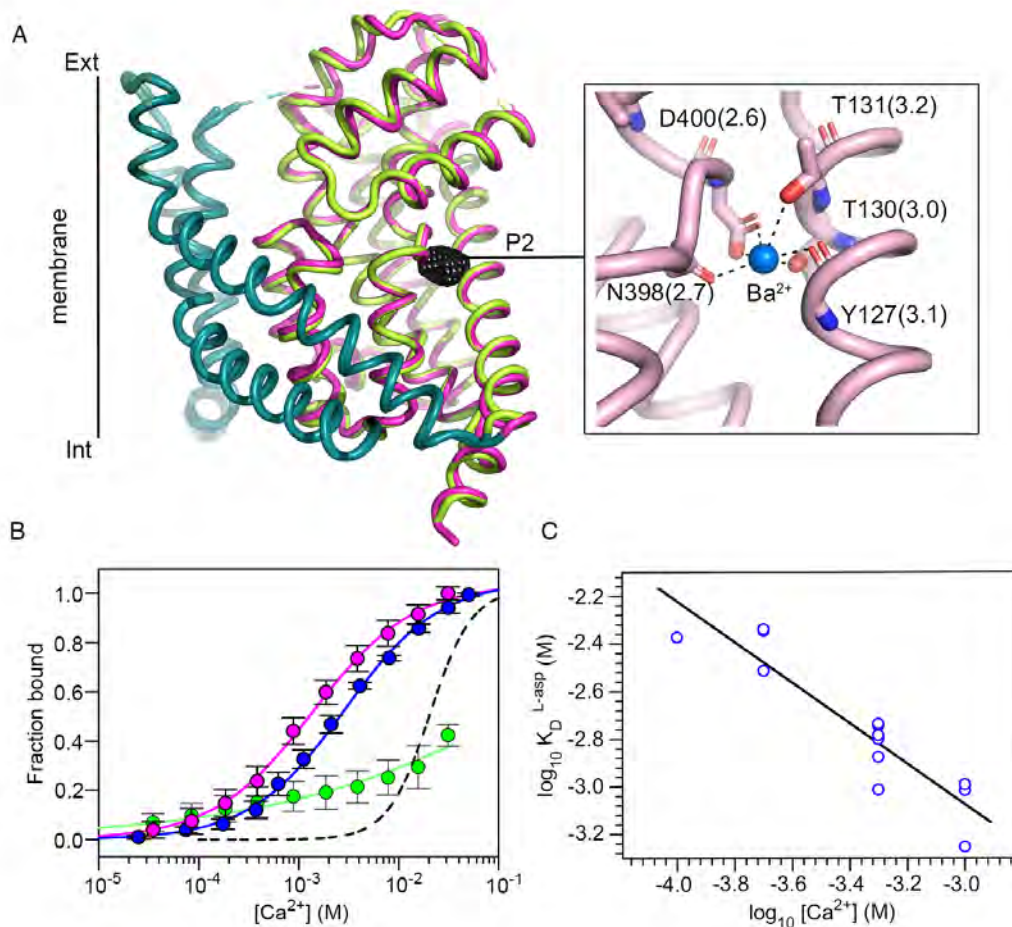
**Figure 4 Counter-transported ion binding site**

935 A. Purified EAAT1<sub>CRYST</sub> takes up L-glutamate in liposomes loaded with K<sup>+</sup> or Rb<sup>+</sup>, but  
936 not with choline (Ch<sup>+</sup>), or with Ch<sup>+</sup> and Ca<sup>2+</sup>. Plots depict data as in Fig. 3A.

937 B. Superimposition of Na<sup>+</sup>/transmitter and Rb<sup>+</sup> bound EAAT1<sub>CRYST</sub> structures,  
938 respectively, with tranD depicted in orange (Na<sup>+</sup>/transmitter) and pink (Rb<sup>+</sup>). TM4 and  
939 UCPH<sub>101</sub> are omitted for clarity. Black mesh depicts anomalous-difference map  
940 contoured at 3.5σ around the tranD. Rb<sup>+</sup> coordination is shown in the inset. Residue  
941 numbering corresponds to EAAT1<sub>WT</sub>, and the coordination distance (angstrom) is  
942 parenthesis.

943 Data information: in (A) bar plots depict averages and s.e.m. values of three  
944 independent experiments (empty circles) performed in triplicate.

945



946  
 947  
 948  
 949  
 950  
 951  
 952  
 953  
 954  
 955  
 956  
 957  
 958  
 959  
 960  
 961  
 962

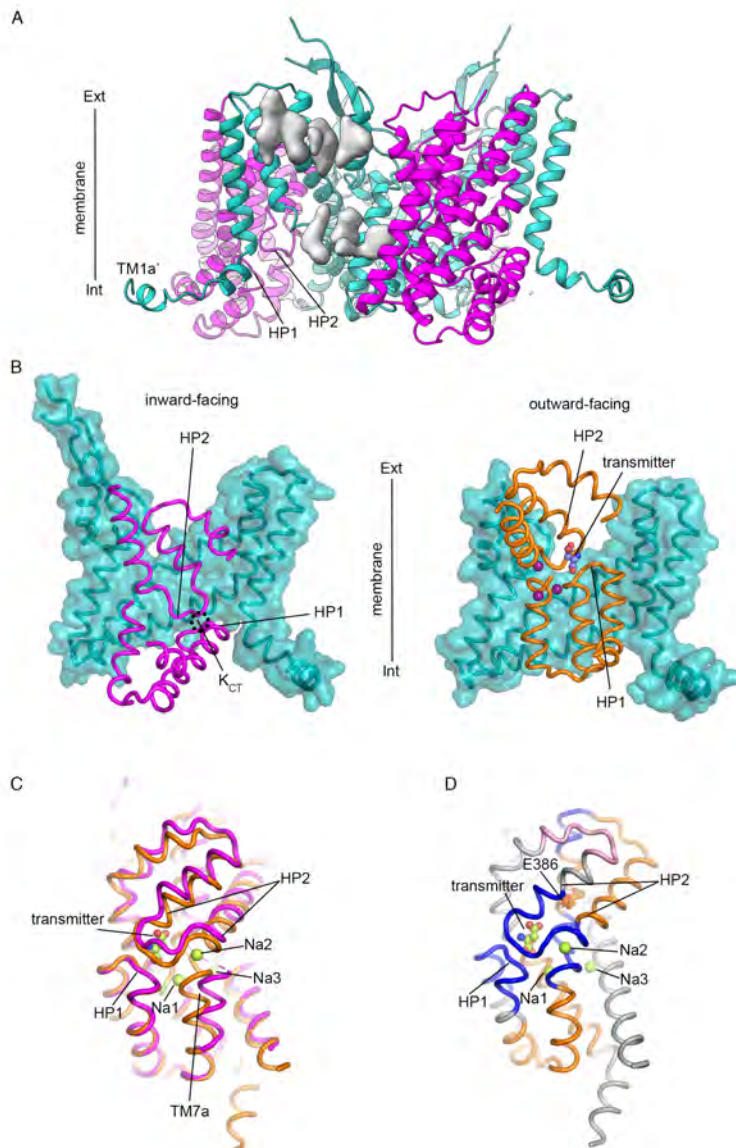
**Figure 5 Divalent cation binding**

A. Superimposition of  $Rb^+/Ba^{2+}$  and  $Ba^{2+}$  bound EAAT1<sub>CRYST</sub> structures with tranD depicted in pink and green, respectively, and TM4 removed for clarity. Black mesh depicts anomalous-difference map in the absence of  $Rb^+$  contoured at  $4\sigma$  around the tranD, and inset shows details of  $Ba^{2+}$  coordination at Na3. Residue numbering corresponds to EAAT1<sub>WT</sub>, and the coordination distance (angstrom) is parenthesis.

B.  $Ca^{2+}$  binding isotherms of EAAT1<sub>CRYST</sub> at pH=7.4 in the presence (pink) and absence (blue) of UPCH<sub>101</sub>. Mutation D400<sub>380</sub>N at Na3 strongly impairs  $Ca^{2+}$  binding (green). Symbols represent average and s.e.m. values of at least three independent experiments. Solid lines represent fits of Hill equation and dashed line is the fit in Fig. 1C (blue line) corresponding to  $Na^+$  binding.

C. Log-log plot of L-asp  $K_D$  as a function of  $Ca^{2+}$  ( $n=13$ ).

Data information: in (B) symbols represent average and s.e.m. values of at least three independent titrations. In (C), blue symbols represent individual  $K_D$  values from  $n$  number of independent titrations.



963  
 964  
 965  
 966  
 967  
 968  
 969  
 970  
 971  
 972  
 973  
 974  
 975

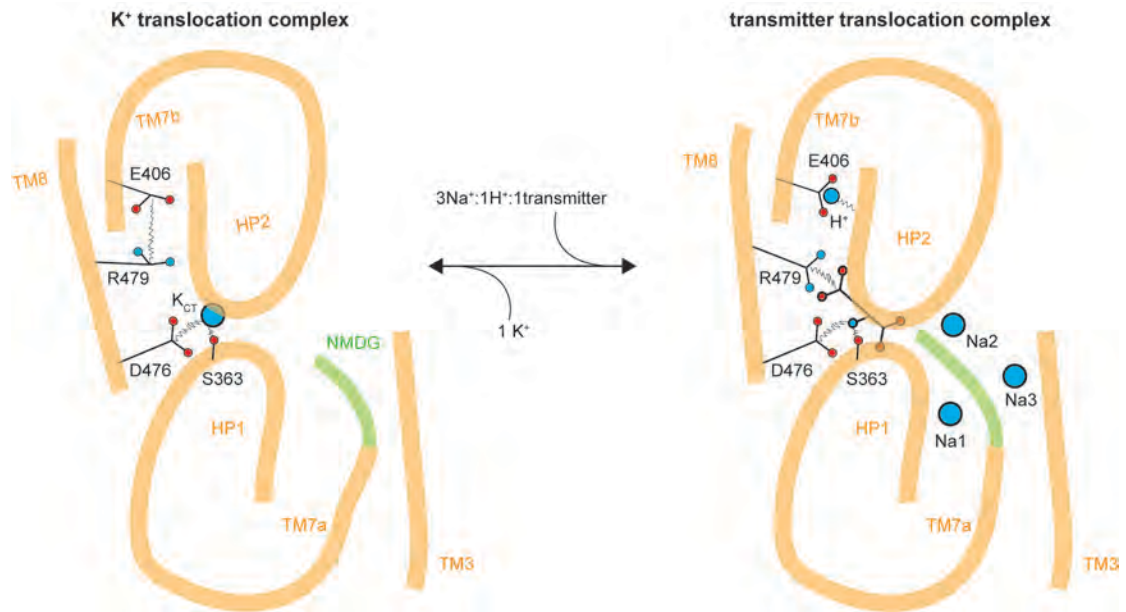
**Figure 6 CryoEM structure and HDX-MS changes in K<sup>+</sup> buffer**

A. CryoEM structure of EAAT1<sub>WT</sub> trimer with tranDs and scaDs depicted in magenta and teal, respectively. Non-protein extra density corresponding to lipid/detergent molecules is depicted in grey.

B. Comparison of EAAT1<sub>WT</sub> (left) and EAAT1<sub>CRYST</sub> (right) structures in inward- and outward-facing states, respectively. Several TMs were removed for clarity.

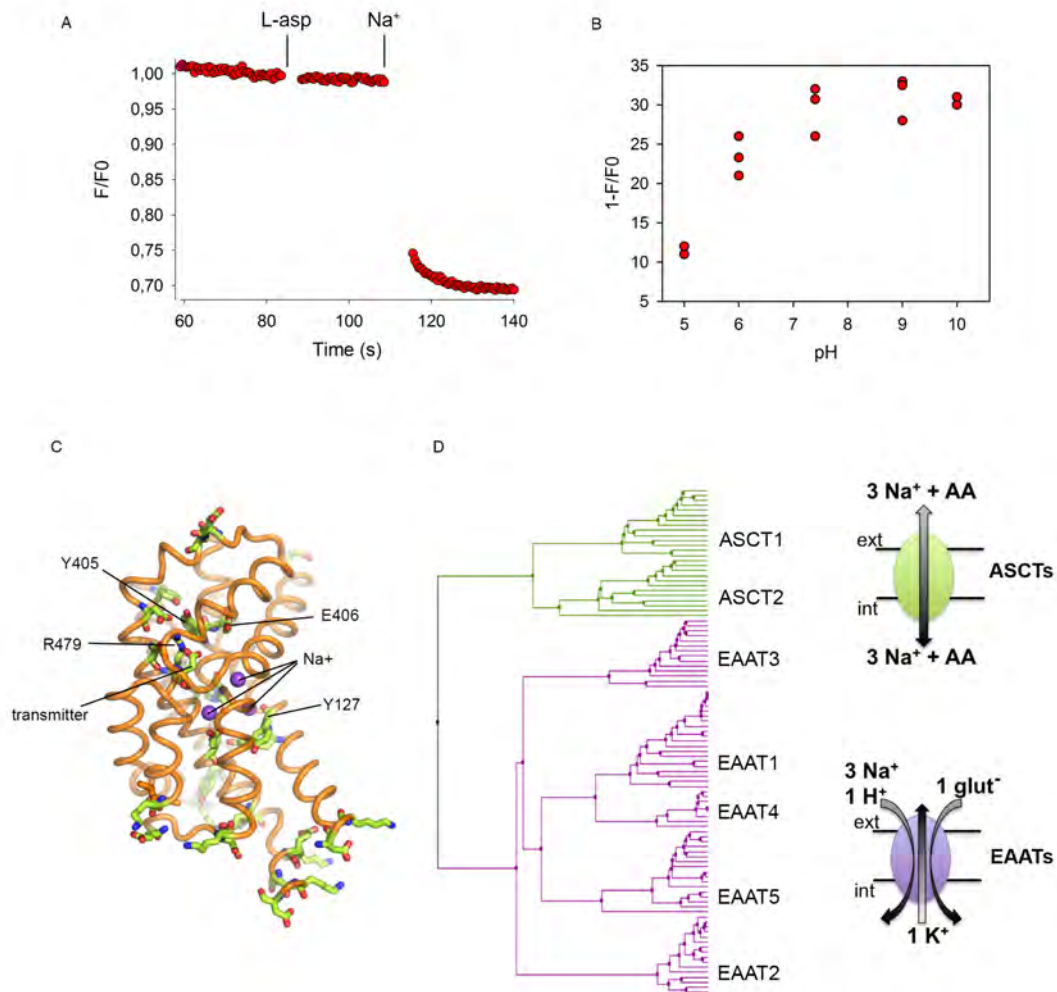
C. TranDs from EAAT1<sub>WT</sub> (magenta) and EAAT1<sub>CRYST</sub> (orange) structures are overlapped using HP1 as reference.

D. K<sup>+</sup>-induced HDX increase (blue) and decrease (pink) in EAAT1<sub>CRYST</sub> is mapped on Na<sup>+</sup>/transmitter-bound tranD structure. Unchanged regions (orange) and those outside HDX-MS sequence coverage (grey) are also shown.



976  
 977  
 978  
 979  
 980  
 981  
 982

**Figure 7 EAAT1  $3\text{Na}^+/\text{H}^+/\text{K}^+$  coupled transport mechanism**  
 Cartoon representation of  $\text{Na}^+/\text{H}^+/\text{transmitter}$ , and  $\text{K}^+$  translocation complexes, respectively.



983  
 984  
 985  
 986  
 987  
 988  
 989  
 990  
 991  
 992  
 993  
 994  
 995  
 996  
 997

**Figure EV1 Proton binding to conserved ionizable sidechain in EAAT<sub>CRYST</sub>**

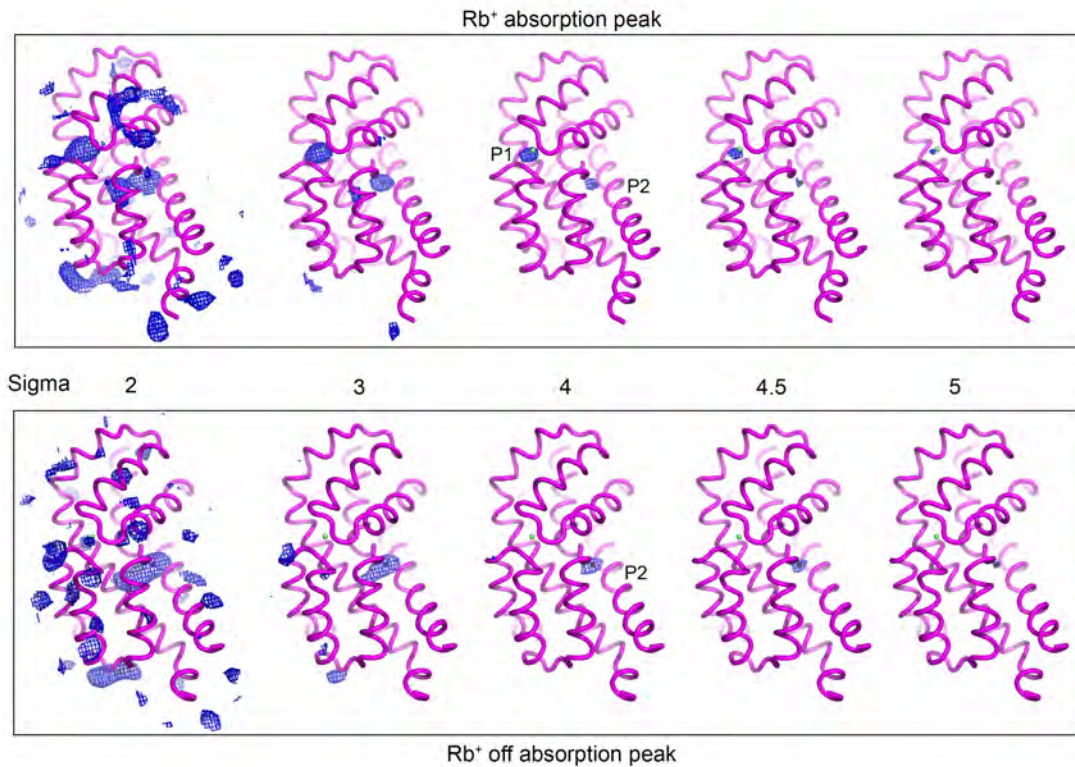
A. EAAT1<sub>CRYST</sub> tryptophan-fluorescence time-course at pH 10 upon addition of saturating concentrations of L-asp, and Na<sup>+</sup>.

B. Percentage of L-asp/Na<sup>+</sup> induced total fluorescence change (1-F/F<sub>0</sub>) decreases at pH values below neutral.

C. Out of >30 ionizable sidechains (green sticks) in the tranD of EAAT1<sub>CRYST</sub> only four (labelled with residue number) are strictly conserved in EAATs, and not in ASCTs.

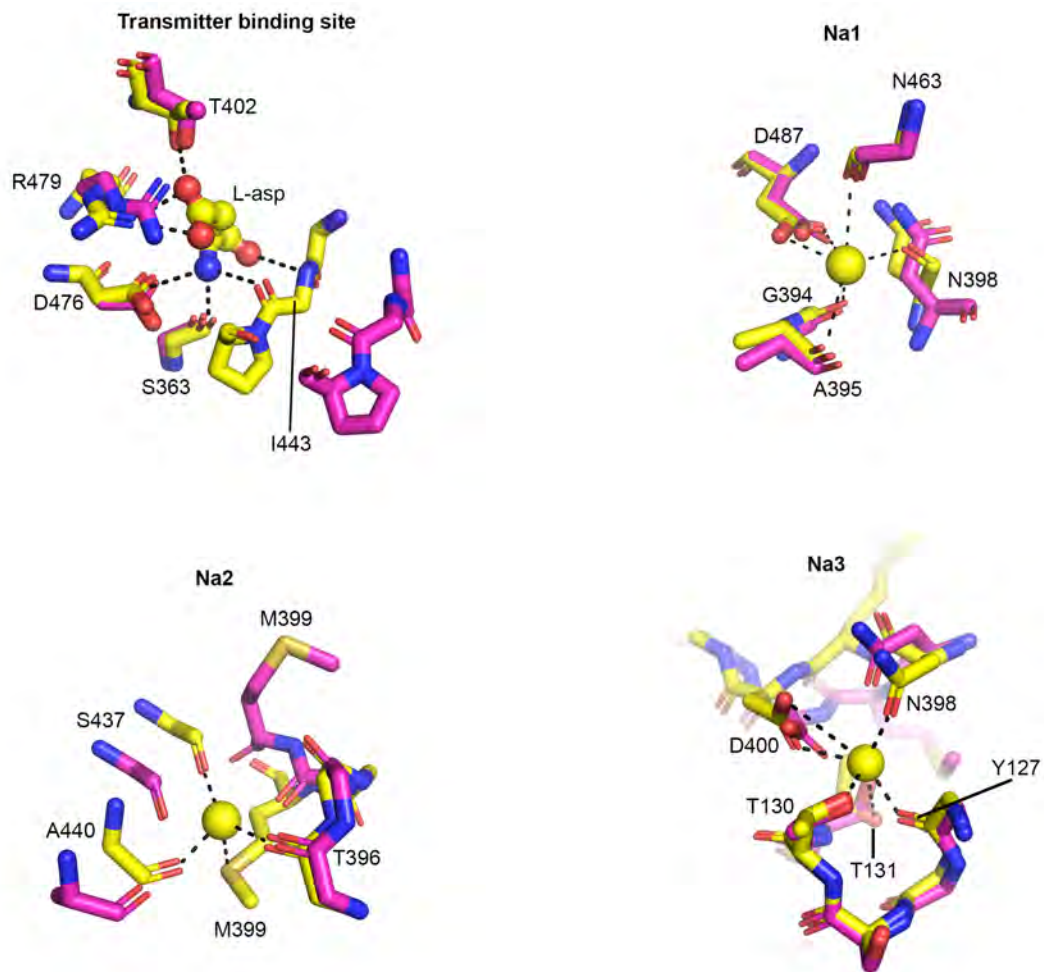
D. Phylogenetic tree from 101 tranD sequences of representative vertebrate species (Gesemann *et al.*, 2010) calculated with Jalview (BLOSUM62 average distance).

Transport stoichiometry of EAATs and ASCTs vertebrate proteins is depicted in cartoon representation.



998  
 999  
 1000  
 1001  
 1002  
 1003  
 1004  
 1005

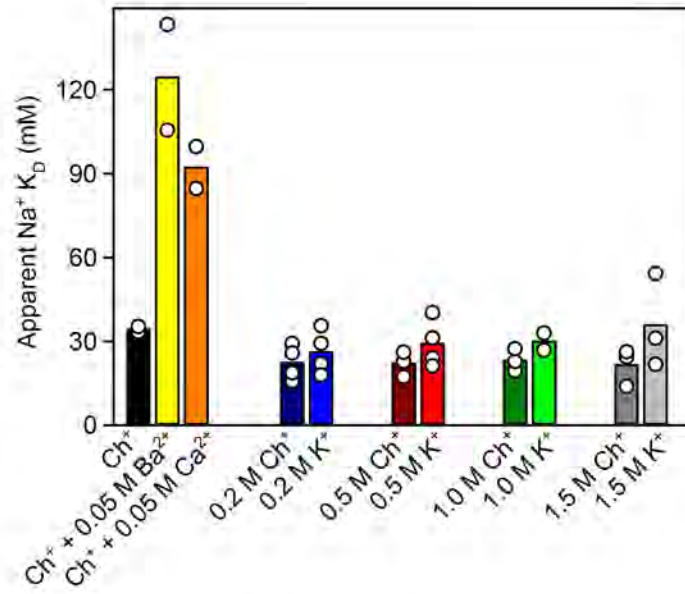
**Figure EV2 Anomalous difference maps of Rb<sup>+</sup>/Ba<sup>2+</sup>-bound structure.** Comparison of anomalous difference maps of Rb<sup>+</sup>/Ba<sup>2+</sup>-bound EAAT<sub>CRYST</sub> structure at the Rb<sup>+</sup> absorption maximum (0.815 Å), and that of EAAT<sub>CRYST-II</sub> off the Rb<sup>+</sup> absorption maximum (0.998 Å). Maps are contoured at increasing sigma levels around the tranD. Rb<sup>+</sup> (green sphere), and Ba<sup>2+</sup> (black sphere) bound to the transporters are depicted.



1006  
 1007  
 1008  
 1009  
 1010  
 1011

**Figure EV3 Transmitter and sodium binding sites in Na<sup>+</sup>/transmitter- and Rb<sup>+</sup>-bound structures**

Conformational re-arrangements around the transmitter and three Na<sup>+</sup> binding sites in Na<sup>+</sup>/transmitter- (yellow) and Rb<sup>+</sup>-bound (pink) EAAT<sub>CRYST</sub> structures.



1012

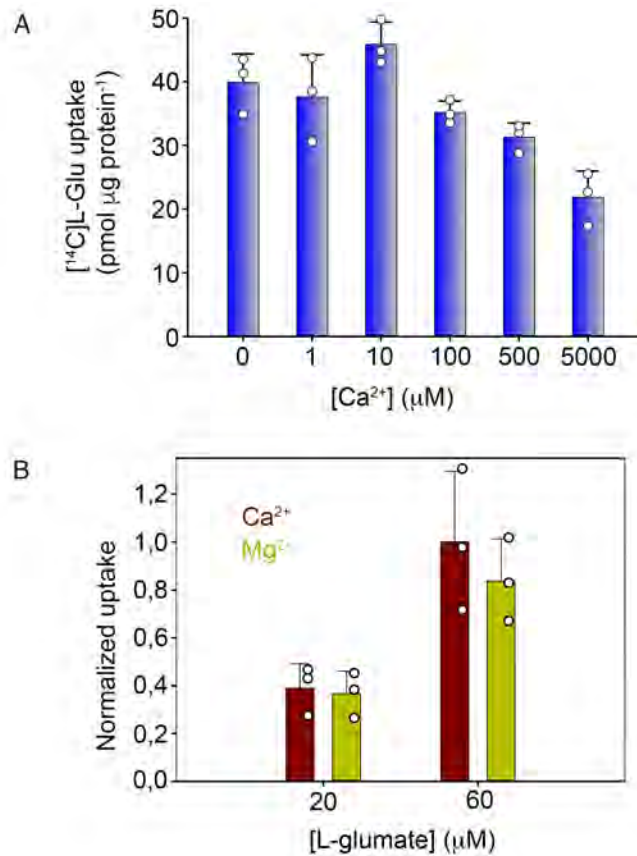
1013 **Figure EV4 Na<sup>+</sup> titrations in different ionic conditions**

1014 EAAT1<sub>CRYST</sub> apparent Na<sup>+</sup> K<sub>D</sub> significantly increased upon addition of 50 mM Ba<sup>2+</sup>  
 1015 or Ca<sup>2+</sup> to a choline (Ch<sup>+</sup>)-based cuvette buffer, but were not modified when Ch<sup>+</sup> in  
 1016 the buffer was substituted for K<sup>+</sup> at concentrations up to 1.5 M. Bar plots present  
 1017 average of at least two independent experiments (empty circles).

1018

1019





1020

1021 **Figure EV5 Ca<sup>2+</sup> effect on steady-state transmitter transport**

1022 A. Effect of intra-liposomal Ca<sup>2+</sup> on L-glutamate transport in the presence of opposite  
1023 gradients of Na<sup>+</sup> and K<sup>+</sup>.

1024 B. Effect of 5mM extracellular Ca<sup>2+</sup> on L-glutamate transport in cells expressing  
1025 EAAT1<sub>CRYST</sub>. There was not significant change in Na<sup>+</sup>-induced L-glutamate uptake  
1026 upon substitution of extracellular Ca<sup>2+</sup> for Mg<sup>2+</sup>, a divalent cation that does not induce  
1027 changes in Trp fluorescence or compete for Na<sup>+</sup> (not shown).

1028

1029

1030

1031

1032

1033

1034

1035

1036

1037

1038

1039

1040

1041